ADVANCED ENERGY MATERIALS
www.advenergymat.de

Discerning Performance Bottlenecks of State-of-the-Art Narrow Bandgap Organic Solar Cells

*Atul Shukla, Manasi Pranav, Guorui He, J. Terence Blaskovits, Davide Mascione, Yonglin Cao, Yufei Gong, Drew B. Riley, Julian A. Steele, Eduardo Solano, Alexander Ehm, Mohammad Saeed Shadabroo, Ardalan Armin, Safa Shoaee, Dietrich R. T. Zahn, Yongfang Li, Lei Meng, Felix Lang, Denis Andrienko, and Dieter Neher**

Discerning loss mechanisms in organic solar cells with narrow optical bandgap is critical for the development of conventional and next-generation photovoltaic technologies, especially for tandem and semi-transparent solar cells. Here, all photocurrent losses are quantitatively deconvoluted in two low-bandgap ($E_g \approx 1.23$ eV) binary systems using structurally analogous non-fullerene acceptors (NFAs), namely BTPV-4F-eC9 and BTPV-4Cl-eC9. Bias-dependent free charge generation and photoluminescence studies pinpoint geminate charge transfer (CT) state recombination as the predominant photocurrent limitation in both systems, compared to parent Y6-blends. Transient absorption spectroscopy too reveals a critical competition between CT decay and separation dynamics. Theoretical calculations uncover multiple stable molecular conformers that restrict NFA aggregation, aligning with morphological studies, resulting in poor CT separation in photoactive blends. Owing to CT loss pathways, free charge recombination in both low-bandgap systems is closer to the Langevin limit than in PM6:Y6. Nonetheless, they exhibit overall voltage losses of ≈0.56 V comparable to PM6:Y6, and efficient exciton dissociation despite a lower driving force. Current–voltage simulations show that suppressing geminate losses can vitally balance recombination pathways to unlock photocurrent potential of low-bandgap blends. Further optimization of the charge carrier mobility would push the PCE >16%, moving the internal quantum efficiency toward the detailed balance limit.

1. Introduction

Driven by the rapid development of organic absorber materials, especially the emergence of non-fullerene acceptors (NFAs), state-of-the-art organic solar cells (OSCs) have reached certified power conversion efficiencies (PCE) of 20%, approaching the performance of their inorganic and perovskite counterparts.[1–6] All of these high-performance blends exhibit photovoltaic bandgaps, E_{PV}, between 1.35 and 1.45 eV, which is ca. 100 meV above the optimum bandgap of the detailed balance (db) prediction. This has been rationalized by significant non-radiative voltage losses in OSCs, which requires a high bandgap to guarantee a high enough open circuit voltage, V_{OC}. However, in recent years several low-bandgap NFAs have gained widespread attention for their applications in tandem solar cells,[7–11] thereby pushing the efficiency potential of OSCs up when paired with an appropriate wide-gap perovskite or organic subcell.[12–14]

A. Shukla, M. Pranav, G. He, D. Mascione, M. S. Shadabroo, S. Shoaee, F. Lang, D. Neher
Institute of Physics and Astronomy
University of Potsdam
Karl-Liebknecht-Str. 24–25, 14476 Potsdam-Golm, Germany
E-mail: neher@uni-potsdam.de

J. T. Blaskovits, D. Andrienko
Max Planck Institute for Polymer Research
Ackermannweg 10, 55128 Mainz, Germany

Y. Cao, S. Shoaee
Paul-Drude-Institut für Festkörperelektronik
Leibniz-Institut im Forschungsverbund Berlin e.V. Hausvogteiplatz 5–7, 10117 Berlin, Germany

Y. Gong, Y. Li, L. Meng
Institute of Chemistry
Chinese Academy of Sciences
2 North 1st Street, Haidian, Beijing 100190, China

D. B. Riley, A. Armin
Sustainable Advanced Materials (Sêr SAM)
Centre for Integrative Semiconductor Materials (CISM)
Department of Physics
Swansea University
Singleton Park, Swansea SA1 8EN, UK

J. A. Steele
Australian Institute for Bioengineering and Nanotechnology
The University of Queensland
Brisbane, Queensland 4072, Australia

The ORCID identification number(s) for the author(s) of this article can be found under https://doi.org/10.1002/aenm.202502398

DOI: 10.1002/aenm.202502398

Combined optical-electrical simulations predicted that an E_{PV} of around 1.2 eV would be ideal for the organic subcell in combination with a perovskite high bandgap top cell in a hybrid tandem device.[12,15,16] The development of NFAs with narrow bandgap has been mainly driven by multiple molecular engineering approaches.[9,10,17–19] For example, Lee et al. designed and synthesized a series of NFAs with bandgaps ranging from 1.34 to 1.20 eV through side-chain engineering.[17] In other work, Hai et al. developed a Y6 derivative, BTPV-4F, with a reduced optical bandgap (1.21 eV) by extending the vinylene π-bridges between the central fused core and the end group.[19] Nonetheless, the resulting PCE of OSC blends based on BTPV-4F and its derivatives are still limited to 14.2% in single-junction and 22% in tandem solar cells.[9,20] Importantly, the efficiency losses relative to the detailed balance limit stems from losses in all photovoltaic parameters – a significant reduction in photocurrent as well as losses in fill-factor (FF) and V_{OC} (see Figure S1a,b Supporting Information). In fact, with two exceptions,[9,21] the average short-circuit current density (J_{SC}) for a bandgap of ca. 1.2 eV notably lies below 28 mA cm^{-2} compared to the db prediction of 39 mA cm^{-2}, as shown in Figure S1a (Supporting Information).[12,22]

Photocurrent losses in OSCs can arise from various factors. One prominent cause is insufficient absorption of incident photons, primarily due to reflection and parasitic absorption. Experiments and optical simulations have shown that absorption losses can easily reach up to 20%.[23,24] To address this, recent high-efficiency reports have employed additional measures such as antireflection coatings[25,26] and light-trapping structures to minimize optical losses.[27] However, even when photons are absorbed and generate local excitons (LEs), these excitons may decay to the ground state before reaching the donor:acceptor (D:A) interface via diffusion. Moreover, even the LE states that reach the D:A interface may not necessarily dissociate completely into charge-transfer (CT) states. We and others have shown that the rate of LE dissociation (i.e., the charge generation rate) can be outcompeted by the intrinsic decay of the LE state—particularly when the driving force for charge generation, $\Delta E_{\mathrm{LE-CT}}$ (the energy offset between the LE and CT state) is low.[28–33] Photocurrent losses through inefficient LE dissociation have been documented for a wide range of NFA-based OPV blends, even for NFAs with relatively long decay lifetimes of the LE state such as Y6 and its derivatives.[28,34] The strong correlation between LE dissociation efficiency and $\Delta E_{\mathrm{LE-CT}}$ has been quantitatively explained by the dependence of the charge transfer rate on $\Delta E_{\mathrm{LE-CT}}$, as described by Marcus theory or its extended versions.[28,32,34–36] A typical signature of the competition between LE dissociation and its decay is the anticorrelation between charge generation and photoluminescence.[28,31,33,37] Some studies, however, suggested that charge generation can still be efficient even in low-offset systems, and instead propose that CT separation—the dissociation of interfacial CT states into free charges—is the limiting step. It has also been proposed that CT separation, or charge separation, becomes increasingly difficult as $\Delta E_{\mathrm{LE-CT}}$ decreases.[38,39] To explain the correlation between the efficiency of charge separation and $\Delta E_{\mathrm{LE-CT}}$, the concept of hot (non-relaxed) CT state formation and separation was employed.[40–42] Here, LE dissociation in a high offset system primarily generates higher energy CT states, which split more easily. However, work by Nakano et al. revealed no correlation between the efficiency of photocurrent generation and the energy difference between the CT state and the charge separated state (CS).[32] Additionally, other studies involving wavelength-selective excitation of fullerene- and NFA-based blends provided little to no evidence of preferential free charge generation via higher-energy (hot) CT states.[43–46]

Irrespective of whether CT recombination is relevant in the process of charge generation, it will be an important if not the dominant channel of non-geminate recombination (described by the recombination coefficient k_{rec}) of free charge carriers and related current losses.[47,48] Indeed, most low-bandgap OSCs incur large non-radiative losses adding to the V_{OC} penalty. Further, other recombination pathways including surface recombination and Shockley–Read–Hall trap-assisted recombination can also play a performance-determining role in the total V_{OC} loss.[11,49,50] Hence, identifying and disentangling charge generation, charge separation, and exciton decay dynamics as well as the total contribution of these voltage loss pathways is critical toward understanding the overall performance metrics of low-bandgap NFA-based OSC.

In this contribution, we perform a comprehensive and quantitative investigation of generation and loss mechanisms in two low-bandgap NFA-based OSCs ($E_g \approx 1.22$ eV) based on state-of-the-art blends combining the polymer donor PTB7-Th and either BTPV-4F-eC9 or BTPV-4Cl-eC9. These NFAs share the same conjugated core but with different halogenated terminal substitutions. We employ a combination of steady-state and time-resolved optoelectronic techniques to deconvolute the efficiency of each intermediate step between photon absorption and charge carrier collection, and assess their impact on the photovoltaic parameters of the two low-bandgap OSCs. Our bias-assisted experiments on free charge generation and photoluminescence show that although CT formation is as efficient as in PM6:Y6, bias-dependent geminate CT losses are the limiting factor for the free charge generation efficiency for both low-bandgap OSCs. This is in contrast to previous reports of LE dissociation being the pivotal step in several NFA-based OSCs,[29–31] and may also be the cause of higher bimolecular recombination coefficients compared to PM6:Y6 blends. This is further confirmed with transient absorption spectroscopy: upon NFA excitation, we find that the decay of the CT state feature competes with the slow rise of the electro-absorption signal generated by the charge separated state. We attribute the poor CT dissociation yield to relatively inhibited NFA aggregation in the D:A blends, as evidenced by morphological studies.[30,45,47] This appears to be a consequence of the extended vinylene π-bridges in these NFAs that afford greater rotational freedom and stable molecular conformers, as

J. A. Steele
School of Mathematics and Physics
The University of Queensland
St Lucia, Brisbane, QLD 4072, Australia
E. Solano
NCD-SWEET Beamline
ALBA Synchrotron Light Source
Cerdanyola del Vallès, Barcelona 08290, Spain
A. Ehm, D. R. T. Zahn
Semiconductor Physics and Research Center for Materials
Architectures and Integration of Nanomembranes (MAIN)
TU Chemnitz, 09107 Chemnitz, Germany

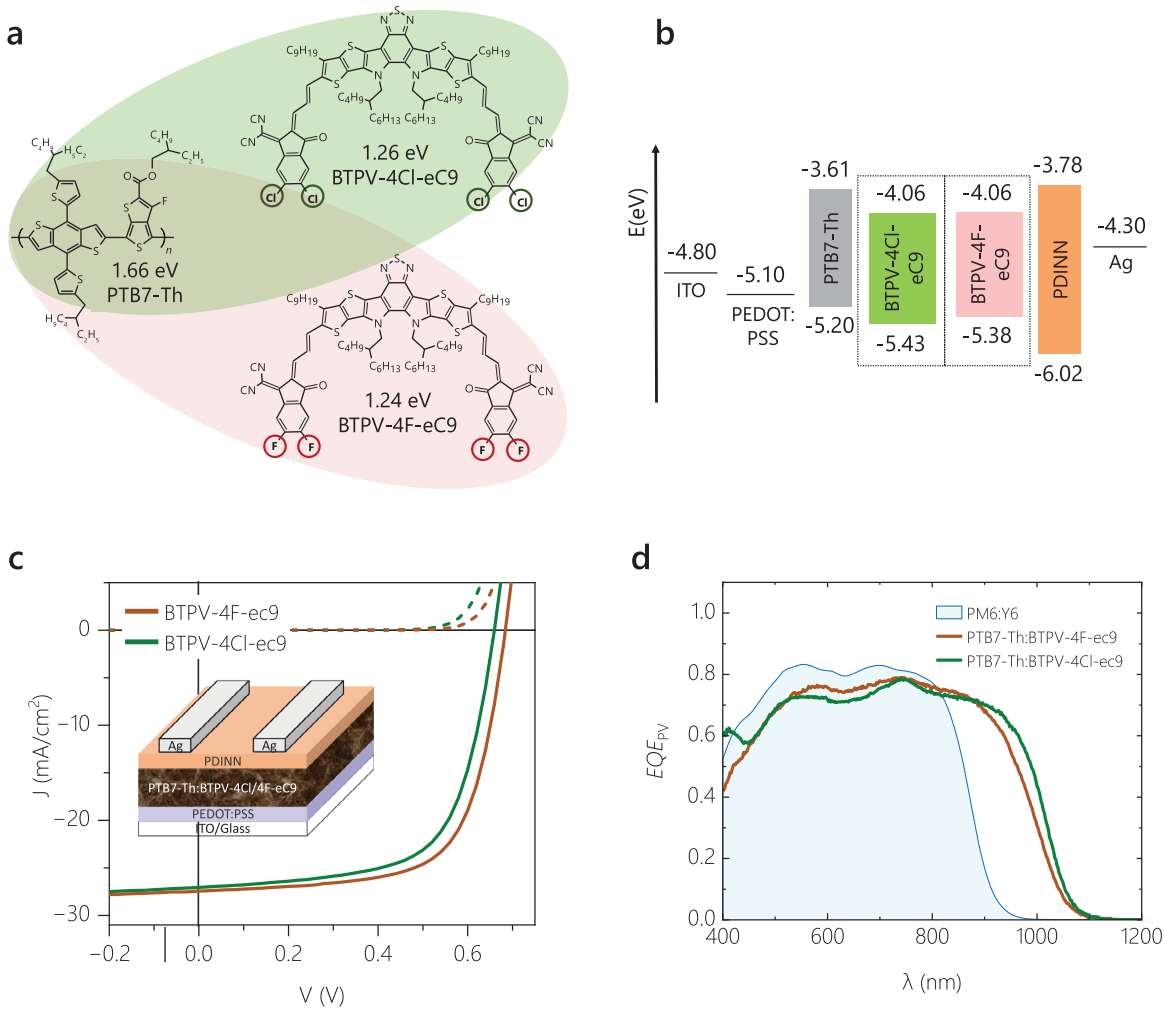

Figure 1. Introducing the low-bandgap photovoltaic model systems. a) Chemical structures and optical bandgaps of the donor polymer, PTB7-Th, and two NFA small molecules, BTPV-4Cl-eC9 and BTPV-4F-eC9. b) Energy diagram of the device stack used in this study. The energy levels of PTB7-Th, BTPV-4Cl-eC9, and BTPV-4F-eC9 were taken from ref.[20,52] and,[51] respectively,[53,54] using cyclic voltammetry of the neat components, c) *J–V* curves of the optimized bulk-heterojunction OSCs based on PTB7-Th:BTPV-4Cl-eC9 and PTB7-Th:BTPV-4F-eC9 under illumination (solid lines, AM 1.5G, 100 mW cm^{-2}) and in the dark (dashed lines). The inset illustrates the conventional device structure. d) External quantum efficiency (EQE_{PV}) spectra of the optimal devices based on PTB7-Th:BTPV-4Cl-eC9 and PTB7-Th:BTPV-4F-eC9. The EQE_{PV} spectrum of a PM6:Y6 OSCs with same device structure is also included for comparison.

demonstrated through quantum mechanical calculations. While previous works have shown the critical role of the molecular quadrupole tensor on CT separation, the lack of long-range order in these low-bandgap blends negates the potential benefits of the NFA quadrupole moment despite it being higher than that of Y6. Lastly, our *JV* simulations confirm the critical role of geminate losses in unlocking photocurrent potential of these low-bandgap systems as per detailed balance.

2. Results and Discussion

2.1. Device Characteristics

The active layers are based on a binary blend of the donor polymer **PTB7-Th**, with NFA **BTPV-4Cl-eC9** or **BTPV-4F-eC9**, with chemical structures and optical bandgaps shown in **Figure 1a**. The optical bandgap was determined by the intersection of the emission and absorbance spectra of neat layers, see Figure S2a (Supporting Information). Figure 1b shows the energy levels of the device components, taken from literature.[20,51] In low-bandgap NFA-based OSCs, the offset between the ionization energy levels (IE) of the corresponding D and A components is often used to approximate the driving force (ΔE_{LE-CT}) for charge generation. The PTB7-Th:BTPV-4Cl-eC9 blend exhibits a marginally higher IE offset as compared to PTB7-Th:BTPV-4F-eC9 based blend. Recent works have shown that reducing the IE offset between the donor and acceptor below ca. 0.3 eV reduces the LE dissociation efficiency.[28,30,34] However, the method for accurate energy level estimation of photoactive OSC blends has been a matter of debate in the OSC community, and therefore the given IE offset in Figure 1b should be considered with care. The conventional

Table 1. Summary of photovoltaic performances of OSCs based on PTB7-Th:BTPV-4Cl-eC9 and PTB7-Th:BTPV-4F-eC9 measured under AM 1.5G, 100 mW cm^{-2} illumination with the PCE of the champion device given in brackets.

System	V_{OC} [V]	J_{SC} [mA cm^{-2}]	FF [-]	PCE[a)]$_{avg}$ (max) [%]
PTB7-Th: BTPV-4Cl-eC9	0.65 ± 0.01	26.8 ± 0.5	0.63 ± 0.01	11.2 ± 0.23 (11.7)
PTB7-Th: BTPV-4F-eC9	0.68 ± 0.01	27.3 ± 0.4	0.67 ± 0.01	12.4 ± 0.21 (12.7)

[a)] Average values from 23 devices.

device structure used in this study is included in the inset of Figure 1c. The low-bandgap active layer blends were sandwiched between the hole transport layer (HTL) PEDOT:PSS and the electron transport layer (ETL) PDINN. Preparation details are given in the Supporting Information.

In this work, we utilized the same additive, annealing temperature and solvent as reported in literature for the PTB7-Th:BTPV-4F-eC9 system and then optimized its device performance by slightly changing the additive concentration and active layer thickness (see Figure S3, Supporting Information and fabrication description in the SI for further details).[10,51] To compare both systems, the exactly same fabrication process was applied to the PTB7-Th:BTPV-4Cl-eC9 system. The PTB7-Th:BTPV-4F-eC9 system showed comparatively better photovoltaic performance than PTB7-Th:BTPV-4Cl-eC9, with champion devices giving a PCE of 12.7% as shown in **Table 1** and Figure 1c. This is consistent with the previously reported PCE for this system (see Figure S4 Supporting Information for the statistics of the photovoltaic parameters).[51] As seen in Figure S1a (Supporting Information), this efficiency is representative of state-of-the-art OSCs in the bandgap range of 1.22 eV, with only one report of higher performance (using a selenophene derivative of BTPV-4F with E_g ≈ 1.17 eV). However, the performance metrics of the OSCs based on BTPV-4X-eC9 NFAs still lag significantly behind the detailed balance limit shown in Figure S1 (Supporting Information). Major reductions in performance not only originate from V_{oc} and FF losses but also from considerable photocurrent losses. The external quantum efficiency (EQE_{PV}) spectra of both low-bandgap OSCs shown in Figures 1d and S5 (Supporting Information) exhibit a broad response from 370 to 1100 nm, in accordance with the corresponding absorption spectra (see Figure S6, Supporting Information), but overall, barely reach 80%.

In the following sections, we present a step-by-step analysis of all loss mechanisms. We compare these losses with the optical and transport losses in PM6:Y6 devices. The molecular structure, absorption spectra and photovoltaic properties of the PM6:Y6 OSC are shown in Figure S7 (Supporting Information). Amongst the wide library of NFAs, Y6 with an optical bandgap of ca. 1.4 eV is one of the most well-studied material systems in recent years.[22,55] When blended with a suitable polymeric donor in bulk heterojunction (BHJ) configuration, OSCs based on Y6 exhibit a V_{OC} above 0.8 V. This system exhibits near unity charge generation yields with activationless free charge generation at a relatively low driving force of 350 meV, along with low voltage losses.[24,45] Using the same device structure, this popular system gives only marginally lower J_{SC} than the low-bandgap systems but with higher V_{OC}. With a modest FF of 66%, our PM6:Y6 OSC yielded a PCE of 13.6%. This is mostly due to a lower fill factor of our devices. We note that higher efficiencies were reported for this system with use of solvent additives and a third active layer component.[55] Here, we intentionally use an as-cast PM6:Y6 blend OSC with relatively weak aggregation in order to compare with the low-bandgap blends that also exhibit poor aggregation properties, as we will show in the following section.

2.2. Molecular Properties and Morphology

The subpar performance of the low-bandgap blends raises the question whether this stems from inherent molecular properties of the NFAs. Therefore, we first investigated possible differences in the conformation profiles of Y6 and its π-extended derivative, BTPV-4F-eC9, with density functional theory (DFT) calculations at the CAM-B3LYP(D3BJ)/def2-SVP level.[56–62] To increase computational tractability, we used molecular structures with the linear and branched side-chains truncated to ethyl and isobutyl, respectively (see **Figure 2**a,b). Figure 2c shows the energy profiles of the relaxed dihedral scans in the single vinyl rotor of one arm of Y6, as well as in both of the vinyl rotors on one arm of BTPV-4F-eC9, which we term the inner dihedral (the exocyclic single bond nearest to the core) and outer dihedral (further from the NFA core). The planar "C"-shaped conformer (labeled as the 0° dihedral) was identified as the most stable conformer for both compounds. The inner dihedral of BTPV-4F-eC9 has the lowest energy barrier of the three dihedrals examined and the coplanar conformer (≈180° for the inner dihedral relative to the C-shaped conformer) of BTPV-4F-eC9 is almost as stable as its starting conformer (1.6 kcal mol^{-1} higher, see Figure 2c). Conversely, the outer dihedral of BTPV-4F-eC9 has a relatively higher rotational barrier while the other non-C-shaped conformers of Y6 are energetically much less favorable. As a result, the C-shaped conformer of Y6 is strongly preferred, compared to the multiple conformational preferences of BTPV-4F-eC9, which has a relatively flatter energy profile. These results clearly demonstrate the possible co-existence of more than one conformation in BTPV-4F-eC9, indicating better miscibility and lower aggregation tendencies. Interestingly, we note that BTPV-4F-eC9 possesses a marginally higher quadrupole tensor than Y6 along the π-π stacking direction (Q_{zz}) (95-103 Debye-Å depending on the conformer, compared to 87 Debye-Å for Y6, see SI Figure S8, Supporting Information). However, its impact on interfacial electrostatics is anticipated to be weak. This can be attributed to structural disorder, including the coexistence of multiple molecular conformers and inadequate NFA aggregation, supported vide infra by morphological studies. This is because the band bending at the D:A interface is primarily driven by the combination of two key factors: (1) the molecular quadrupole moments of NFAs[63] and (2) the concentration gradient of donor and acceptor species between the

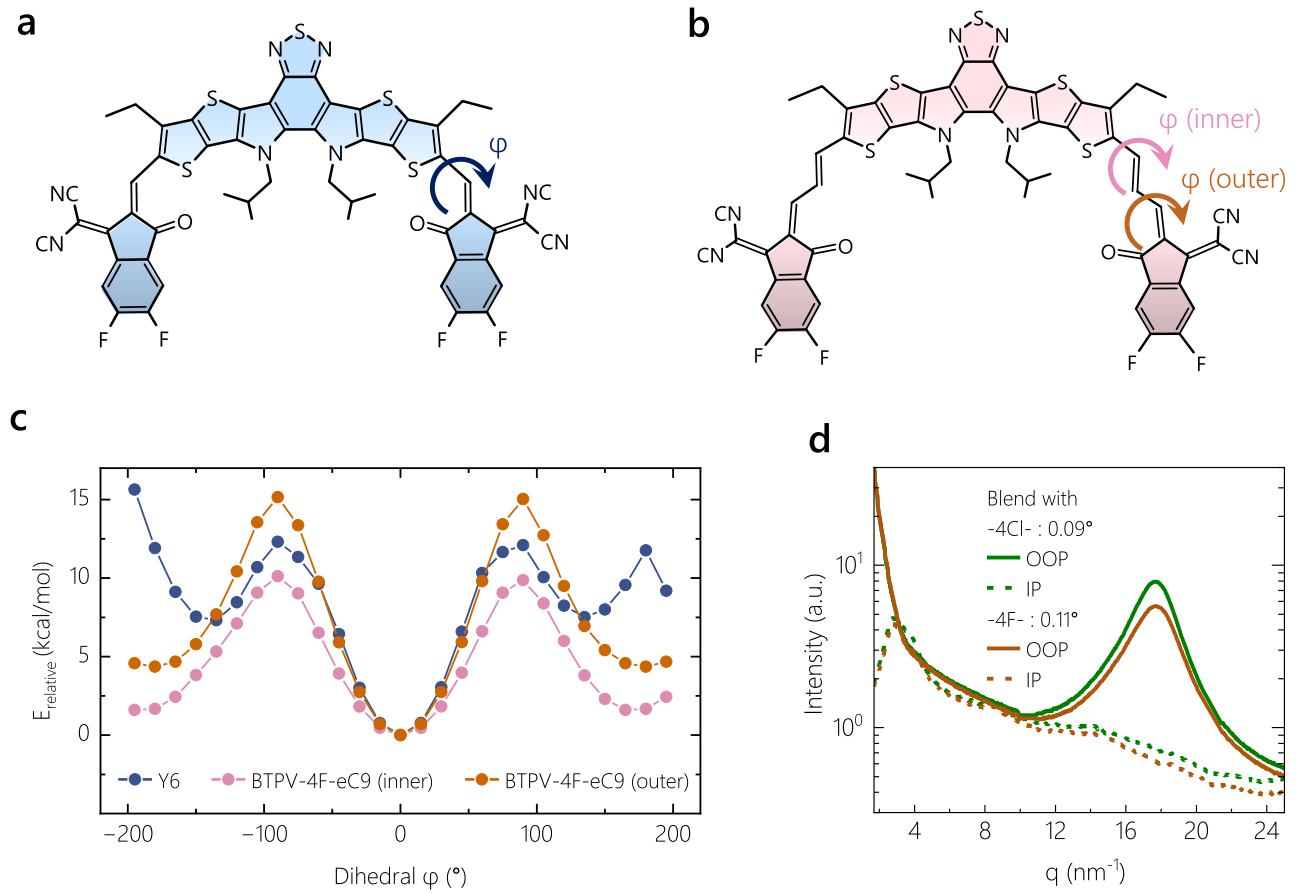

Figure 2. Revealing stable molecular conformers of low-bandgap NFA and their impact on morphology. Molecular structures of a) Y6 and b) BTPV-4F-eC9 with truncated side chains used to compute conformational energies. The vinyl rotors along which the dihedral scans are performed are indicated by arrows. c) Energies of the molecular conformers of each acceptor molecule at various dihedral angles φ on the vinyl rotors marked with arrows in the chemical structures, relative to the lowest energy conformers at dihedral $\varphi = 0°$. For both compounds, the molecular conformation for $\varphi = 0°$ of the respective vinyl groups corresponds to the C-shaped structures shown in a) and b). d) The out-of-plane (OOP) and in-plane (IP) line-cut profiles from the GIWAXS images for PTB7-Th:BTPV-4F-eC9 and PTB7-Th:BTPV-4Cl-eC9 at an optimal incident angle of 0.09 and 0.11°, respectively.

interfacial and bulk regions. While the higher Q_{zz} values for BTPV-4F-eC9 are favorable for the quadrupole induced electrostatic interactions, its disrupted aggregation characteristics reduce the concentration gradient between the interface and the bulk. These findings closely align with the recent work by Fu et al. on molecular orientation-dependent energetic shifts in Y6, in which the authors demonstrated that Y6 films processed from chloroform exhibited reduced energetic shifts due to relatively looser packing along the π-π stacking direction compared to those processed from chlorobenzene.[64] It is anticipated that the intermolecular interaction of mixed molecular conformations of BTPV-4F-eC9 (see Figure S8, Supporting Information) might also induce higher disorder in photoactive blends.

Our theoretical findings were further validated by absorption spectroscopy on Y6 and BTPV-4F-eC9 in THF:hexane solvent mixtures. This solvent combination was selected due to good solubility of the NFAs in THF and their moderate solubility in hexane. At high THF fractions, both NFAs exhibit a well-structured vibronic spectrum consistent with the Franck-Condon progression (see Figure S9 Supporting Information). For Y6, increasing the hexane fraction results in the emergence of a new low-energy peak at 870 nm (1.54 eV), which we attribute to Y6 aggregates.[65] In contrast, BTPV-4F-eC9 maintains a well-resolved vibronic structure of the non-aggregated state across all THF:hexane mixtures, with no additional contribution from aggregated species. This suggests improved miscibility and reduced aggregation tendencies of BTPV-4F-eC9 relative to Y6, aligning with our theoretical predictions.

With the knowledge from theory, we investigate the nano- and microscale morphology of the two blend systems. The crystalline features of the low-bandgap blend films were investigated using synchrotron grazing incidence wide-angle X-ray scattering (GIWAXS).[66] The GIWAXS patterns with diffraction intensity at different azimuthal angles and q value are shown in Figure S10a,b (Supporting Information) with more details, and the corresponding integration profiles ($\Delta\chi = 10°$) in the out-of-plane (OOP) and in-plane (IP) directions are shown in Figure 2d. The blend films based on both low-bandgap systems display preferred face-on orientation with a π-π stacking peak at around q ≈ 17.7 nm^{-1} in the OOP direction and a lamellar peak at around q ≈ 2.80 nm^{-1} in the IP direction, which is consistent with previous findings.[19] As listed in Table S1, we find marginally larger

crystalline coherence length (CCL) of PTB7-Th:BTPV-4Cl-eC9 in OOP (2.51 nm) as well as IP direction (7.57 nm) in comparison to 2.33 nm in OOP and 5.92 nm in IP direction of the PTB7-Th:BTPV-4F-eC9, indicating the formation of slightly larger crystalline domain of acceptors in the PTB7-Th:BTPV-4Cl-eC9 blend films. However, as will be discussed in Sections 2.3 and 2.4, the shorter LE decay lifetime of BTPV-4Cl-eC9, along with the enhanced acceptor crystallinity in the PTB7-Th:BTPV-4Cl-eC9 blend, leads to overall reduction in LE dissociation efficiency for this blend system.

The topographic features of the two systems were examined using atomic force microscopy (AFM) on active layers on glass.[67] The AFM height images, as displayed in Figure S10c,d (Supporting Information) for both low-bandgap systems, indicate smooth surfaces and root-mean-square roughness S_q<1, S_q = 0.70 nm and S_q = 0.98 nm for the chlorinated and flourinated NFA-blend, respectively. Our previous morphological studies with PM6:Y6 have revealed phase separation with domains lengths of ≈20 nm, rendering higher S_q values ranging between 1.5-2 nm due to the formation of large Y6 crystal domains.[49,68–71] These results indicate a more disordered morphology for PTB7-Th:BTPV-4F-eC9 and PTB7-Th:BTPV-4Cl-eC9 based systems compared to higher-performing PM6:Y6, which is expected due higher available conformational freedom in BTPV-4X-eC9.[28,72]

2.3. Quantitatively Discerning Photocurrent Loss Pathways

In the following, we perform a step-by-step analysis of all photocurrent losses. These steps are illustrated in **Figure 3b** along with their corresponding efficiencies. To this end, we introduce different photocurrent densities that progressively describe what the steady-state device photocurrent would be in the absence of each stepwise loss channel. Hereby, we extend the approach introduced by Collins and co-workers[73] by explicitly taking bias-dependent exciton dissociation into account. The photocurrent densities thus defined are namely,

- the device photocurrent density, $J_{ph}(V) = J_{light}(V) - J_{dark}(V)$: the contribution of photogenerated charge carriers to the total device current measured after all loss channels,
- the reverse saturation photocurrent density, $J_{ph,sat}$: measured at high reverse bias, when all bias-dependent losses during free charge generation and extraction are absent,
- the free charge (FC) generation photocurrent density, $J_{ph,FC}$: if there are no extraction losses ($\eta_{coll} = 1$),
- the CT generation photocurrent density, $J_{ph,CT}$: if every CT state formed at a D:A interface produced an electron in the external circuit ($\eta_{coll} = \eta_{CT,d} = 1$),
- the LE generation photocurrent density, $J_{ph,LE}$: if every photogenerated LE state produced an electron in the external circuit ($\eta_{coll} = \eta_{CT,d} = \eta_{LE,d} = 1$) (note that $\eta_{LE,d}$ includes both LE dissociation and LE diffusion), and lastly,
- the maximum photocurrent density J_{max}: the hypothetical value if every step-by-step efficiency including absorption would be unity ($\eta_{coll} = \eta_{CT,d} = \eta_{LE,d} = \eta_{abs} = 1$) and which, if all else is consistent, approaches the db limit.

Figure 3a,d shows the photocurrent density J_{ph}(V) from *JV* measurements of the BTPV-4F-eC9 and BTPV-4Cl-eC9-based blends. For both systems, J_{ph}(V) displays a considerable bias dependence over almost the entire voltage range studied here, which approaches a constant value of ≈ca. 29.7 mA cm^{-2} only at high reverse bias. We denote this as the reverse saturation photocurrent density $J_{ph,sat}$, as described above. Interestingly, the slope of J_{ph}(V) is still significant around short-circuit (SC), in contrast to PM6:Y6. It has been proposed that such a slope arises from a photoshunt, related to the transport resistance of the active layer.[74] In the following, we show that while non-geminate recombination (NGR) indeed contributes to the non-zero slope around SC, a major contribution arises from bias-dependent free charge generation.

We determined the bias-dependence of free charge generation and the corresponding photocurrent density, $J_{ph,FC}$(V), in both systems using time-delayed collection field (TDCF) measurements.[45,75] In TDCF, we carefully extract all the free charge that was photogenerated in the presence of an electric field but in the absence of NGR (i.e., when $\eta_{coll} = 1$). Figure S11a,b (Supporting Information) summarizes the temporal evolution of charges generated at different bias conditions (pre-bias) of both low-bandgap systems, which were then collected with a high reverse bias potential (collection bias = −7 V) in TDCF. The number of generated free charge carriers at each pre-bias condition over the number of incident photons yields the external generation efficiency (EGE). Figure S11c (Supporting Information) presents the normalized EGE for both low-bandgap systems and for PM6:Y6. The low-bandgap OSCs show a considerable bias-dependence in the positive bias range compared to at −2 V, whereas the EGE for PM6:Y6 is completely bias-independent as reported before.[45] To rule out pseudo-first order recombination between photogenerated and dark-injected charge carriers that could possibly reduce the number of extractable photogenerated charge (and therefore EGE) at positive pre-biases, we verified the bias-dependence recorded from classical TDCF (cTDCF) with the recently developed modified-TDCF technique (see the SI and references[37] and[76] for more details on modified-TDCF). Accordingly, we find this loss process to be of insignificance to the classical TDCF results, as deduced from the overlapping bias-dependent EGE results from both TDCF techniques for the two low-bandgap systems in SI Figure S11c (Supporting Information). Thereafter, we use the bias-dependent EGE over a broader bias range of both low-bandgap systems to calculate their $J_{ph,FC}$(V), using the method described in SI Note S1 (Supporting Information). As shown in Figure 3a,d, we find that $J_{ph,FC}$(V) shows the same bias dependence as J_{ph}(V) over a wide bias range, including around SC, for both low-bandgap systems. It is only at positive bias, when the internal built-in field is compensated, that J_{ph}(V) deviates strongly from $J_{ph,FC}$(V) which is indicative of charge extraction losses due to NGR in the low-field range.

We proceeded to identify whether the bias-dependence of $J_{ph,FC}$(V) originates from inefficient charge generation (LE dissociation) or charge separation (CT separation). In recent work on different NFA-based blends, we identified the former process as the main cause of photocurrent loss, especially at small IE offsets.[28,29,31] Therein, this was proven by a pronounced bias-dependence of the photoluminescence quantum yield (*PLQY*), which perfectly anticorrelated with that of the EGE. Following this deconvolution approach, $PLQY_{D:A}$(V) was herein obtained for each low-bandgap blend by normalizing the peak intensities

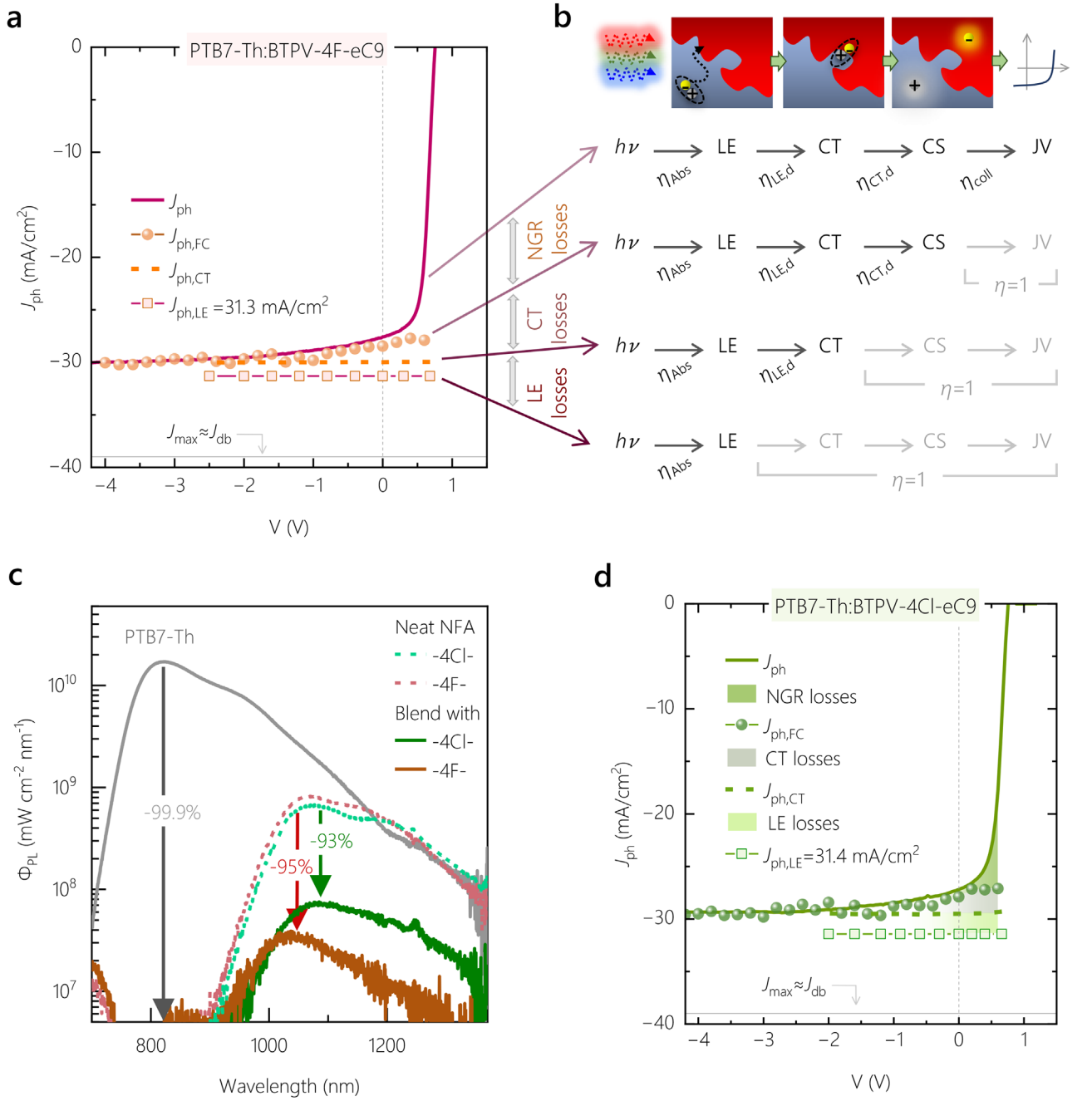

Figure 3. Quantifying the stepwise reduction in photocurrent between absorbed photon and collected electron. a) Bias-dependent photocurrent densities from *JV* (J_{ph}) measured under simulated AM1.5G light (solid line), overlaid with $J_{ph,FC}$ (circles, the photocurrent density without extraction losses), and $J_{ph,CT}$ (dotted line, the photocurrent density purely due to LE dissociation assuming perfect charge separation and extraction) for PTB7-Th:BTPV-4F-eC9. Also indicated is the upper limit for photocurrent assuming only absorption losses ($J_{ph,LE}$, squares) and no losses at all (J_{max}). b) An illustration of the photophysical difference between each photocurrent density defined herein. c) The photoluminescence (PL) spectra of the neat films of PTB7-Th, BTPV-4F-eC9 and BTPV-4Cl-eC9 shown in comparison with those the respective blend films. PL quenching values were calculated via (1 – $PLQY_{blend}/PLQY_{donor}$). d) The equivalent of sub-figure a) but for the PTB7-Th:BTPV-4Cl-eC9 system.

of their steady-state PL spectra measured under different applied bias to that at $V = V_{OC}$, and then scaling the dataset to the PLQY of each blend.[28] Note that the PL spectra of each blend at all applied biases show close similarities to the spectral shape of the neat acceptor (see Figures S12 and S13, Supporting Information), meaning that the PL stems almost entirely from the radiative decay of the NFA LE state. Surprisingly, $PLQY_{D:A}$(V) in both low-bandgap OSCs is independent of bias, see Figure S14 (Supporting Information). This rules out inefficient LE dissociation as a source of photocurrent loss, which would be bias-dependent. We

can therefore safely conclude that the bias-dependence of $J_{ph,FC}$ stems from field-assisted CT separation. Hence, the CT generation photocurrent density $J_{ph,CT}$ (when $\eta_{CT,d} = \eta_{coll} = 1$) must be independent of bias and approximately equal to $J_{ph,sat}$, as denoted by the dashed lines in Figure 3a,d. This is in contrast to observations in several NFA-based OSCs, in which LE dissociation is the bottleneck to bias-dependent J_{ph}.[28–30,37]

Consequently, the only other loss pathway afflicting $J_{ph,CT}$ would be via (bias-independent) competition of LE recombination with its diffusion to the D:A interface. Since donor LE states are almost entirely quenched, most likely due to energy transfer to the acceptor,[30] this particular loss due to inefficient LE diffusion on the NFA is calculated using PL quenching: the comparison of the $PLQY_{D:A}$ of each blend with that of the corresponding neat NFA layers ($PLQY_A$) (See Figure S13 Supporting Information for the spectra, and Figure S15, Supporting Information for the PLQY values). Subsequently, $J_{ph,LE}$ (when $\eta_{LE,d} = \eta_{CT,d} = \eta_{coll} = 1$) for each low-bandgap blend is calculated as the reference for their $J_{ph,CT}$ using the respective PL quenching terms that accounts for inefficient LE diffusion, as described in Note S1 (Supporting Information). The calculated values of $J_{ph,LE}$ = 31.3 and 31.4 mA cm^{-2} for the fluorinated and chlorinated NFA-based blend, respectively, are marked by the square symbols in Figure 3a,d.

We validate $J_{ph,LE}$ with calculations from the simulated active layer absorption in the device stack. This requires the optical constants of the neat acceptor and blend films, which were obtained using variable angle spectroscopic ellipsometry (VASE) (see Supplementary Note S2 and Figure S16, Supporting Information for more details). The neat and blend films of BTPV-4F-eC9 and BTPV-4Cl-eC9 showed strong optical anisotropy, consistent with previous reports of other Y-series derivatives.[77,78] Hence, the calculation of the active layer absorption in the OSC stack was performed using the in-plane anisotropy parameters (See simulation details summarized in Note S1, Supporting Information).[24,79] With this in hand, $J_{ph,LE}$ was predicted by integrating the stimulated absorption of the active layers within the device stack over the AM1.5G spectrum as shown in Figure S17 (Supporting Information). This yields current densities of $J_{ph,LE}$ = 31.6 mA cm^{-2} for PTB7-Th: BTPV-4F-eC9 and 32.7 mA cm^{-2} for PTB7-Th:BTPV-4Cl-eC9, consistent within 5% of the values calculated using PL quenching. Finally, the photocurrent loss due to inefficient absorption ($\Delta J_{abs,\,loss}$) was predicted using the internal quantum efficiency (IQE_{PV}). Figure S18 (Supporting Information) shows the IQE_{PV} values lying below 90% in both low-bandgap OSCs, compared to PM6:Y6 which clearly exhibits IQE_{PV} well over 90% in the entire spectral range, as previously reported.[24,45] We determined this final loss component via $\Delta J_{abs,loss} = \int IQE_{PV}\phi_{AM1.5}d\lambda - \int EQE_{PV}\phi_{AM1.5}d\lambda$, which was found to be 6.1 mA/cm^2 and 5.6 mA/cm^2 for the BTPV-4F-eC9- and BTPV-4Cl-eC9-based blends, respectively. Adding $\Delta J_{abs,\,loss}$ to $J_{ph,LE}$ gives the theoretical maximum photocurrent J_{max} with zero losses. This yields J_{max} within 5% of 39 mA cm^{-2}, which is the expected theoretical maximum J_{SC} for the 1.2 eV bandgap range, thereby proving the consistency of our methodology.

The comparison of $J_{ph,LE}$ and $J_{ph,CT}$ with $J_{ph,FC}$ and J_{ph} provides quantitative information about the pathways for photocurrent loss in these low-bandgap OSCs, as indicated by the schematic in Figure 3b. The progressive reduction in photocurrents after each loss channel for both low-bandgap blends and for PM6:Y6 are tabulated in **Table 2** under SC and maximum power point conditions. The data presented in Figure 3a,d for the BTPV-4F-eC9 and BTPV-4Cl-eC9-based OSCs, respectively, clearly demonstrate how both geminate and non-geminate recombination significantly affect the bias-dependence of their photocurrent. Notably, the curvature of J_{ph} around short-circuit is mimicked by that of $J_{ph,FC}$, showing that bias-dependent CT separation governs the bias-dependence of the device photocurrent. This is likely a consequence of the intermixed morphology afforded by the NFA's multiple conformers. Mixed phases have previously been proposed as a possible source of bias-dependent charge separation in polymer-fullerene blends.[80] In fact, the combination of all D:A interfacial losses reduces J_{SC} by 2.4 mA cm^{-2} from its photocurrent potential (from 30.0 mA cm^{-2} to the measured J_{SC} of 27.6 for the case of the fluorinated low-bandgap OSC), which is a nearly 10% loss.

Using the calculated and measured current densities defined thus far, we are able to assign efficiencies to each fundamental step between incident photon and a free electron appearing in the outer circuit. The absorption efficiency is obtained using $\overline{\eta_{abs}} = \int EQE_{PV}\phi_{AM1.5}d\lambda / \int IQE_{PV}\phi_{AM1.5}d\lambda$ (where $\phi_{AM1.5}$ is the AM1.5 G spectrum). The deviation of $J_{\mathrm{ph,LE}}$ from $J_{ph,CT}$ denotes the loss of photogenerated LE states, such that $\eta_{LE,d} = \frac{J_{ph,CT}}{J_{ph,LE}} <$ 100% at short-circuit is due to inefficient LE diffusion. We denote the CT separation efficiency using $\eta_{CT,d} = \frac{J_{ph,FC}}{J_{ph,CT}}$. Lastly, we estimated the charge collection efficiency with $\eta_{coll} = \frac{J_{ph}}{J_{ph,FC}}$. We summarize these efficiencies that determine the experimental J–V curves of these low-bandgap systems in Table 2. Our analysis of deconvoluting photocurrent losses indeed shows that the limitation to photocurrent in both low-bandgap OSCs compared to PM6:Y6 is primarily due to relatively inefficient CT separation.

2.4. Charge Generation Dynamics in Transient Absorption Spectroscopy

To corroborate the results thus far, we characterized the charge generation process in both low-bandgap systems at ultrafast timescales by deciphering charge and exciton dynamics using transient absorption (TA) spectroscopy. We selectively excited the NFA since recent works showed that charge generation in low-bandgap NFAs mainly relies on hole transfer from the acceptor to the donor, and that excitations on the donor undergo ultra-fast energy transfer to the NFA prior to electron transfer at the D:A interface.[28,30,36]

First, we studied the transitions in pure donor and acceptor phases. Figure S19a (Supporting Information) shows the TA spectra of pristine PTB7-Th film. The negative signal around 650 nm is attributed to the ground state bleach (GSB) of PTB7-Th due to its resemblance with the ground state absorption, while the positive signal around 1280 nm is attributed to the photoinduced absorption (PIA) of the donor LE state. TA spectra of the polystyrene:NFA (PS:NFA) films in Figure S19b,c (Supporting Information) (for the fluorinated and chlorinated NFA, respectively) show a biexponential decay of the NFA GSB (negative feature between 700–1000 nm), with major contributions from a slower decay lifetime of 130 and 91 ps for BTPV-4F-eC9 and

Table 2. Summary of efficiencies and respective current densities at various stages of free charge generation, starting from the efficiency of light absorption in photoactive blend $\overline{\eta_{abs}}$, then that of LE dissociation $\eta_{LE,d}$ and CT splitting under short-circuit (SC) and maximum power point (MPP) conditions $\eta_{CT,d}$, and lastly that of free charge collection η_{coll}. The efficiencies are calculated by correlating data sets from optical simulation, PLQY, TDCF, and *JV* curves, using the equations in the above text and illustrated in **Figure 4a**.

in mA cm^{-2}	$J_{ph,LE}$	$J_{ph,CT}$	$J_{ph,FC}(SC)$	$J_{ph,FC}(MPP)$	$J_{ph}(SC)$	$J_{ph}(MPP)$
PTB7-Th:BTPV-4Cl-eC9	31.4	29.5	27.9	27.1	27.2	22.2
PTB7-Th:BTPV-4F-eC9	31.3	30.0	28.5	28.0	27.6	22.3
PM6:Y6	27.0	25.6	25.6	25.6	24.3	20.4
in %	$\overline{\eta_{abs}}$	$\eta_{LE,d}$	$\eta_{CT,d}(SC)$	$\eta_{CT,d}(MPP)$	$\eta_{coll}(SC)$	$\eta_{coll}(MPP)$
PTB7-Th:BTPV-4Cl-eC9	82%	94%	94%	91%	97%	82%
PTB7-Th:BTPV-4F-eC9	81%	96%	95%	93%	97%	80%
PM6:Y6	84%	95%	100%	100%	95%	80%

BTPV-4Cl-eC9, respectively. We find positive features at 1000–1100 and 520–670 nm, which we assign to PIA from NFA LE states. Both PS:NFA films display an isosbestic point at around 650 nm, which is at the same wavelength where neat PTB7-Th exhibits a strong GSB signal. Hence, the kinetics in this region can be attributed to charge transfer under selective acceptor excitation of both low-bandgap systems. Surprisingly, the NFA PIA feature between 1000–1100 nm decays much more rapidly as compared to the NFA GSB, which may be attributed to the formation of intramoiety CT states, the PIA band of which lies beyond 1300 nm.[81–83] Since our study pertains to charge generation in D:A blends, further discussion on the intramoiety CT state is beyond the scope of this work. Importantly, both acceptors show relatively short LE lifetimes as compared to that of Y6 under the same test conditions (see Figure S20a, Supporting Information). Note that LE lifetimes obtained in TA measurement conditions can be impacted by exciton-exciton annihilation. To probe the intrinsic LE lifetime, bereft of exciton-exciton annihilation effects,[10] we measured the GSB decay of BTPV-4F-eC9 dispersed in polyvinylcarbazole (PVK) at low doping concentration, as shown in Figure S20b (Supporting Information). We obtained a mono-exponential decay lifetime of 378 ps, which is significantly lower than the reported intrinsic exciton lifetimes of Y6 (in the range of 0.7–1.5 ns).[72,84,85] We consider the rather short LE lifetime as one of the reasons for the exciton diffusion losses noted earlier.

The TA spectra of PTB7-Th:BTPV-4F-eC9 and PTB7-Th:BTPV-4Cl-eC9 are shown in Figure 4a,b, respectively. The excitonic transitions of the corresponding PS:NFA films (between 0.3–0.5 ps) are overlaid on top as a guide. Upon selective excitation of the NFAs, both blends show the rise of donor GSB at sub-ps time scales (within the resolution of our measurement setup), suggesting ultrafast hole transfer from acceptor to donor. Notably, nearly half of the charge transfer process is completed within the initial 1 ps. The donor GSB continues to rise with time and peaks at ca. 32 and 43 ps for PTB7-Th:BTPV-4F-eC9 and PTB7-Th:BTPV-4Cl-eC9, respectively. Additionally, a new positive feature arises between 1050–1200 nm, which is attributed to the PIA of the PTB7-Th cation through comparison with PTB7-Th:$PC_{70}BM$ reference films (see Figure S21, Supporting Information). This signal rises concurrently with the rise of the PTB7-Th GSB in both low-bandgap blends, as evidenced from the blends' kinetics in Figure 5c,d. We, therefore, attribute this to charge generation via hole transfer. Figure S22 (Supporting Information) shows a biexponential rise of this charge population in both blends – a similar sub-ps rise due to hole transfer from LEs at interfaces, and a slow rise component limited by the diffusion of LEs in pure acceptor domains to the interface. Herein, the PTB7-Th:BTPV-4Cl-eC9 blend shows a marginally slower rise of the diffusion component, which confirms the presence of relatively larger domain size of the acceptor as compared to PTB7-Th:BTPV-4F-eC9. Interestingly, the kinetics show a delayed rise of another band between 770–900 nm which we assigned to the Stark-shift induced electroabsorption (EA) feature of PTB7-Th due to separated charges.[86]

The hole transfer and charge separation kinetics of the low-bandgap blends are compared with that of PM6:Y6 in SI Figure S23c,d (Supporting Information), referenced against the corresponding donor GSB and EA dynamics, respectively (see TA spectra of PM6:Y6 under selective acceptor excitation in Figure S23a (Supporting Information)), showing PM6 GSB between 580–600 nm and PM6 EA beyond 660 nm,[33] the corresponding dynamics are presented in Figure S23b (Supporting Information). Clearly, while the two low-bandgap acceptors exhibit shorter LE lifetime, the charge generation in these systems remains efficient due to the comparatively fast hole transfer process. The slower hole transfer process in PM6:Y6 is mainly attributed to the LE diffusion process in relatively large Y6 domains (>20 nm).[87] Despite this, PM6:Y6 shows a steeper rise in the donor EA that goes in parallel with charge generation. In contrast, both the low-bandgap blends exhibit a biphasic rise in EA, with a fast component (<100 ps) followed by minor contributions from a slow rise as seen in Figure 4c,d. Herein, by performing two-pool deconvolution on the combined GSB and EA dynamics within initial 100 ps, we obtain quantitative information about the faster CT separation component. The PM6:Y6 system exhibited an ultrafast CT separation time constant of 1.1 ps, whereas blends based on BTPV-4Cl-eC9 and BTPV-4F-eC9 displayed relatively slower separation, with time constants of 11 and 12 ps, respectively. Importantly, the delayed rise in EA of PTB7-Th between 100 ps to 1 ns is concurrent with the decay of the donor GSB and polaron PIA signature, which describes the competition between CT decay and slow CT separation in the low-bandgap systems. The attribution of donor GSB decay to the CT loss pathway is validated with pump-fluence dependent measurements on the PTB7-Th:BTPV-4F-eC9 blend (see Figure S24, Supporting Information), wherein a fluence-independent decay profile at

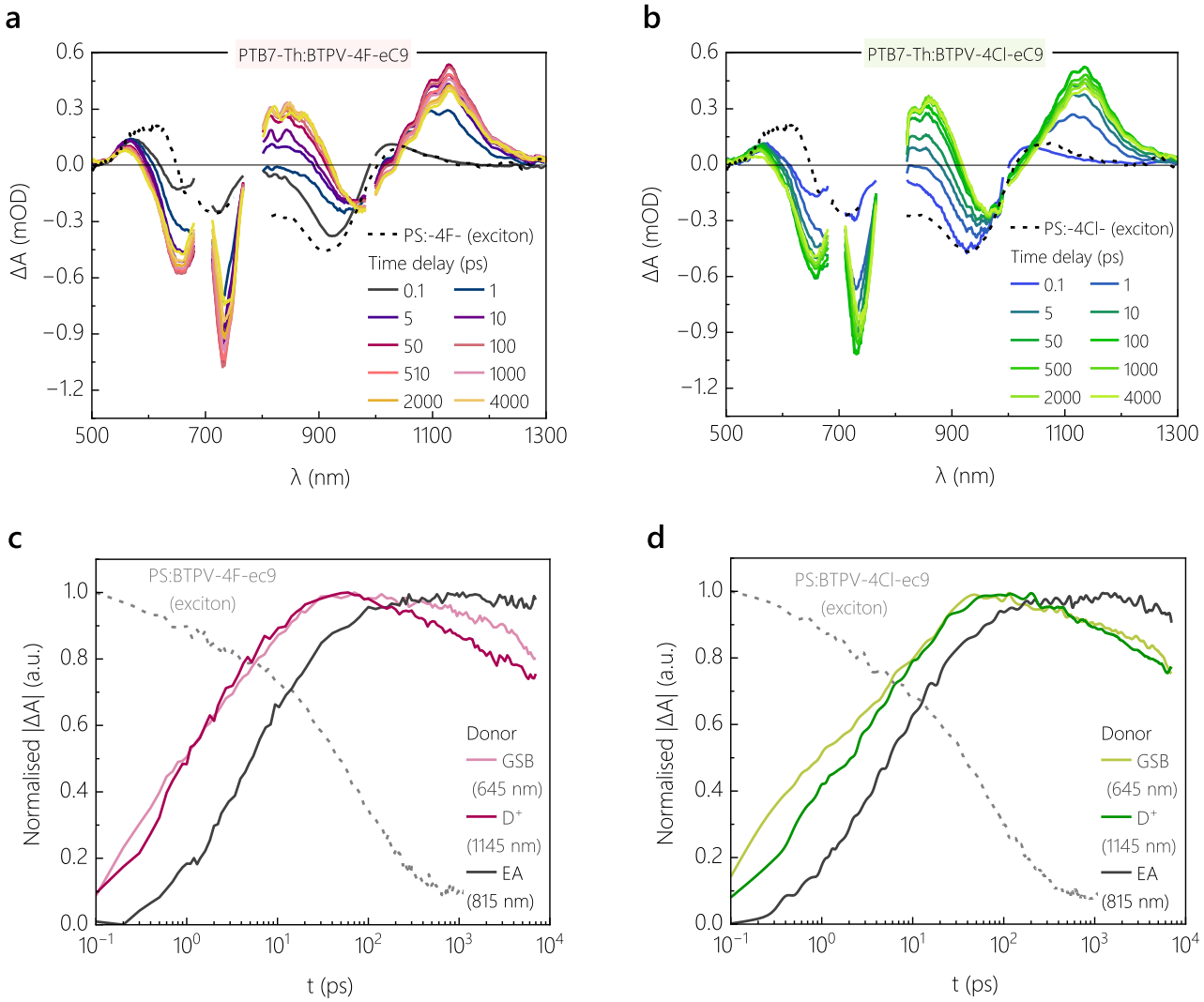

Figure 4. Kinetic competitions of CT state observed in transient absorption timescales. Transient absorption spectra of a) PTB7-Th:BTPV-4F-eC9 and b) PTB7-Th:BTPV-4Cl-eC9 blend films with 820 nm pump excitation of 1.7 μJ cm^{-2} fluence for selective NFA excitation. The black dotted lines denote the optical transitions of the respective PS:NFA films between 0.3–0.5 ps to benchmark the transient spectra of the blends. Transient absorption kinetics at selected wavelengths for c) PTB7-Th:BTPV-4F-eC9 and d) PTB7-Th:BTPV-4Cl-eC9 blend films.

<1 ns confirms monomolecular CT decay. The CT decay time constants, obtained from a fit to the donor GSB decay, are found to be ca. 320 and 360 ps for BTPV-4Cl-eC9 and BTPV-4F-eC9 based blends, respectively. The geminate loss of ca. 10% due to CT decay in this later time range is consistent with the observation of the CT losses in TDCF measurements under open circuit conditions.

To conclude this section, we find rather similar charge generation dynamics in PTB7-Th:BTPV-4F-eC9 and PTB7-Th:BTPV-4Cl-eC9. Their relatively intermixed morphology assists in fast charge generation dynamics at the interface as compared to PM6:Y6 blend. This occurs despite relatively shorter LE decay lifetimes in the low-bandgap materials, whereby LE diffusion losses account for overall <100% efficiency in charge generation. However, the lower tendency of the two low-bandgap NFAs to crystallize results in relatively small acceptor domains in the active layer blends, critically impeding the rate of CT separation. Previous studies on Y6-based blends attributed efficient spatial charge separation to the downhill energy relaxation near the interfaces, facilitated by crystal fields formed due to large acceptor domains via static molecular quadrupole moments.[45,88] The likely lack thereof in BTPV-4F-eC9 and BTPV-4Cl-eC9 inhibits the overall free charge generation process, despite faster charge generation compared to Y6.

2.5. Free Charge Recombination and Energy Losses

To examine how non-geminate recombination (NGR) pathways affect the FF, we utilize charge extraction methods on complete devices, specifically TDCF and Bias-Assisted Charge Extraction (BACE).[46,89–91] Through these techniques, we assess the power-law dependence of the free charge carrier recombination rate (R) on the mobile charge carrier density (n), enabling us to

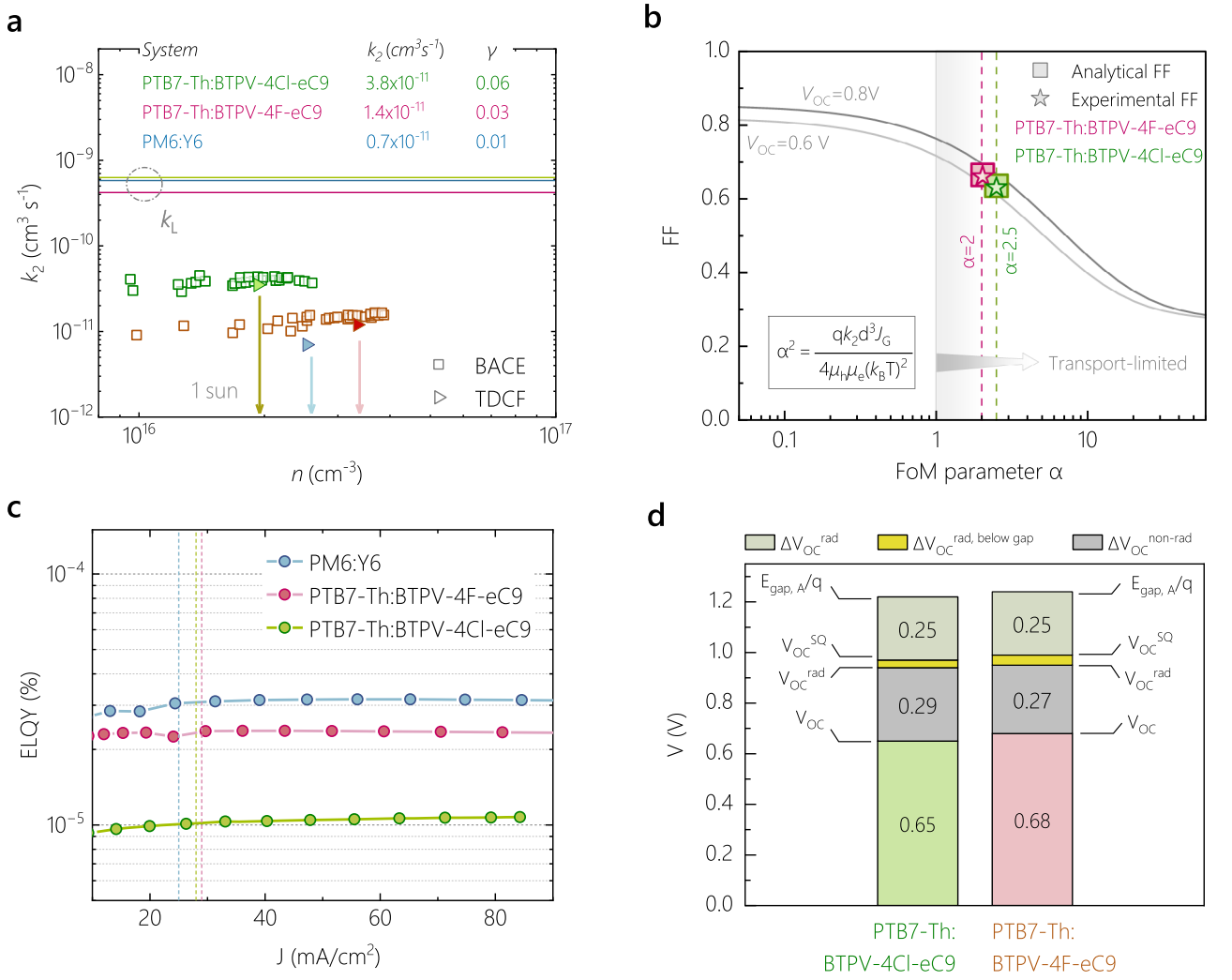

Figure 5. Assessing impact of recombination on FF in low-bandgap systems. a) The carrier density-dependent bimolecular recombination coefficients (k_2) for PTB7-Th:BTPV-4F-eC9 and PTB7-Th:BTPV-4Cl-eC9, as obtained from TDCF and BACE measurements along with the comparison with PM6:Y6. The solid lines indicate the k_2 for Langevin-type encounter-limited recombination (k_L) of free charge carriers. b) The analytical FF obtained with the Neher analytical *JV* model, as a function of the figure of merit α which expresses the balance between charge recombination and extraction. The analytical FF is compared with the experimentally obtained values for both low-bandgap OSCs. c) ELQY values of PTB7-Th:BTPV-4F-eC9 and PTB7-Th:BTPV-4Cl-eC9 systems as compared to PM6, showing comparatively higher non-radiative losses in the two low-bandgap systems. d) A bar graph illustrating the voltage losses for the PTB7-Th:BTPV-4F-eC9 and PTB7-Th:BTPV-4Cl-eC9 blends.

determine the recombination coefficient *k*. Figure S25 (Supporting Information) presents the *R*-vs.-*n* plots obtained using TDCF with iteratively increasing delayed extraction times (t_{del}) after laser excitation (free charge generation) across various incident laser fluences for the two low-bandgap OSCs. Additionally, the *R*-vs.-*n* data from BACE are overlaid, depicted with square markers. Linear fits to the data sets show that both low-bandgap systems display a predominant second-order dependence of *R* on *n*. This instates bimolecular recombination as the dominant loss mechanism and rules out trap-assisted recombination pathways which would yield a lower recombination order. Previous reports have shown that for reduced injection barriers, surface recombination can also exhibit a second-order dependence on carrier density.[92] However, as we will demonstrate in later sections, surface recombination has only a minor impact on these narrow-bandgap OSCs. The corresponding *R*-versus-*n* dependence of PM6:Y6 based OSCs was also measured using TDCF for comparison (Figure S26, Supporting Information). Using the power-law relationship of *R*-vs.-*n* in BACE and TDCF measurements, we calculate the bimolecular recombination coefficient k_2 as depicted in **Figure 5**a. Notably, both low-bandgap systems exhibit higher bimolecular recombination coefficients than PM6:Y6. We attribute this to weaker aggregation of the NFAs that impedes not only charge separation[93,94] but also reduces the energetic barrier to charge encounter.[47] Beyond morphological factors, the lower IE offset can be another plausible reason to higher k_2 of the blends with low-bandgap acceptors.[31]

The second-order dependence suggests that NGR herein is driven by Langevin-type encounter between mobile charge carriers. In the Langevin model, any deviation from the

mobility-limited encounter and recombination of mobile charge carriers can be quantified by the Langevin reduction factor, $\gamma = k_2/k_L$. Here, k_L is the Langevin recombination coefficient and it depends on the sum of the free charge mobilities,[95] which were determined with a combination of resistive photovoltage (RPV)[96] and space-charge limited current (SCLC) measurements (see Experimental Section and Figures S27 and S28, Supporting Information). We find that the measured $k_2's$ are suppressed by more than one order of magnitude from the corresponding $k_L's$ for all three blends, as seen in Figure 5a. According to analytical and numerical considerations, this must be caused by efficient re-splitting of the CT states formed upon free charge formation.[94,95,97] In accordance with this interpretation, the system with the most efficient CT separation, PM6:Y6, exhibits the most suppressed NRG.[94]

To confirm that the *FF* of our devices is mostly governed by NGR, we employed the figure-of-merit α approach formulated by Neher et al., linking FF to transport and recombination characteristics.[98] Here, when α, described by the equation in Figure 6b, approaches values below 1, the system enters the Shockley regime where FF reaches its optimal value for a given V_{OC}, free from transport limitations. In Figure 6b, FF is plotted as a function of α for V_{OC} values of 0.8 and 0.6 V. We superimposed both the experimental FF values and the calculated FF obtained from our experimental data from RPV and TDCF/BACE, and found very good agreement for both systems. PTB7-Th:BTPV-4F-eC9 based OSCs exhibit comparatively less transport-limited behavior, while the greater deviation in photocurrent from ideality in BTPV-4Cl-eC9 based OSCs due to faster charge recombination results in a lower FF.

To lastly quantify the voltage loss in the two low-bandgap systems, we combined the results from electroluminescence quantum yield (ELQY) and electromodulated photoluminescence (EMQL) measurements, with the details of the calculation shown in Supplementary Note S3 (Supporting Information). The total voltage loss, which is quantified as $q\Delta V_{OC}$, can be attributed to three main factors:

$$q\Delta V_{loss} = \left(E_{gap} - qV_{OC}^{SQ}\right) + q\Delta V_{OC}^{rad,belowgap} + q\Delta V_{OC}^{non-rad} \quad (1)$$

When compared to the photovoltaic bandgap, both the blend systems exhibit comparable total voltage losses, with a 46.7% loss in the PTB7-Th:BTPV-4Cl-eC9 system, and 45.1% in PTB7-Th:BTPV-4F-eC9 system. We obtain the same radiative loss for both systems due to detailed balance, and a similar radiative recombination below the gap, $\Delta V_{OC}^{rad,bg}$. The non-radiative voltage loss, as derived from ELQY, is found to be larger for PTB7-Th:BTPV-4Cl-eC9 (see Figure 5c), which can be attributed to the lower bandgap and consequently shorter LE (or CT state) decay lifetime of the acceptor as shown in transient absorption studies. Interestingly, we found that the total non-radiative voltage loss includes a small V_{OC} loss from surface recombination (19 meV in the PTB7-Th:BTPV-4Cl-eC9 and 13 meV in the PTB7-Th:BTPV-4F-eC9 system) as deduced from EMQL measurements (see Figure S29, Supporting Information). This is unlike recent reports on the ultralow-bandgap blend PTB7-Th:COTIC-4F that yielded a significant voltage loss due to surface recombination.[7,99] The summary of the overall voltage loss analysis for the two low-bandgap OSCs alongside PM6:Y6 is shown in **Table 3**. Clearly, OSCs based on both the low-bandgap NFAs show very similar voltage losses of ≈560 meV, comparable to the state-of-the-art PM6:Y6 based OSCs and other high-performing OSCs reported in literature.[100,101] The relatively small difference in the voltage losses of two low-bandgap OSCs and the PM6:Y6 device is surprising given the ca. 160 meV higher photovoltaic gap of the latter, which in accordance to the energy-gap law would reduce the non-radiative voltage losses. This can be in part explained by the slightly (ca. 30 meV) reduced driving force of the low-bandgap OSCs (related to a lower HOMO offset), which compensates for the higher non-radiative voltage losses.[28] The relatively higher k_2 and non-radiative voltage losses for PTB7-Th:BTPV-4Cl-eC9 also suggest a relatively broader distribution of CT energies as shown in previous works.[102] However, combined results for the two low-bandgap blends suggest only minor room for further improvements in the total voltage losses.

2.6. Discussion and Understanding Performance Limits

Through a quantitative discernment of the photon-to-charge loss pathways, we highlight that geminate recombination of the CT state is a major bottleneck limiting the photocurrent in PTB7-Th:BTPV-4F-eC9 and PTB7-Th:BTPV-4Cl-eC9 OSCs. Despite fast CT formation with shorter LE lifetimes as seen in TA analysis, these low-bandgap NFAs perform inferiorly to their parent Y6 in equally unlocking their photocurrent potential as per detailed balance, and lose ca. 28% of their maximum photocurrent at operating conditions. Nevertheless, it is unique that the BTPV-4F-eC9 acceptor generates state-of-the-art BHJ device efficiency in the 1.2 eV bandgap range despite our calculations showing that it exhibits multiple energetically stable conformers. It is likely that the results from our calculations on molecular conformations on this NFA would apply to BTPV-4Cl-eC9 as well. This correlates well with the lack of long-range order and intermixed morphology of this blend compared to PM6:Y6, as supported by morphological studies. By extension, the hindered stacking abilities of this acceptor could further impact charge transport and FF in a photovoltaic blend. We interpret the more disordered morphology as the main reason for the less efficient and bias-dependent dissociation of the CT state, which would otherwise benefit from the comparatively higher quadrupole moment of the acceptor. This further exacerbates the relatively higher bimolecular recombination of these low-bandgaps systems, leaving them with more Langevin NGR and higher FF losses.

At this point we briefly cover the dispute described in the introduction, namely whether or not inefficient CT separation is a general bottleneck for photocurrent generation in NFA-based OSCs, especially for systems with low driving force. Temperature-dependent electroluminescence measurements in a previous study on PTB7-Th:BTPV-4F-eC9 yielded a driving force of ΔE_{LE-CT} ≈90 meV, which is 20–30 meV smaller than for the well-performing PM6:Y6 blend.[28,29,72,88] This may indicate that the bias-dependence of CT separation (which does not exist in PM6:Y6) reported here is related to a smaller ΔE_{LE-CT}. However, previous works with TDCF and PLQY-studies on a PM6:BTPV-4F-eC9 OSC with an even smaller ΔE_{LE-CT} of ca. 50 meV did not show evidence for more severe CT separation

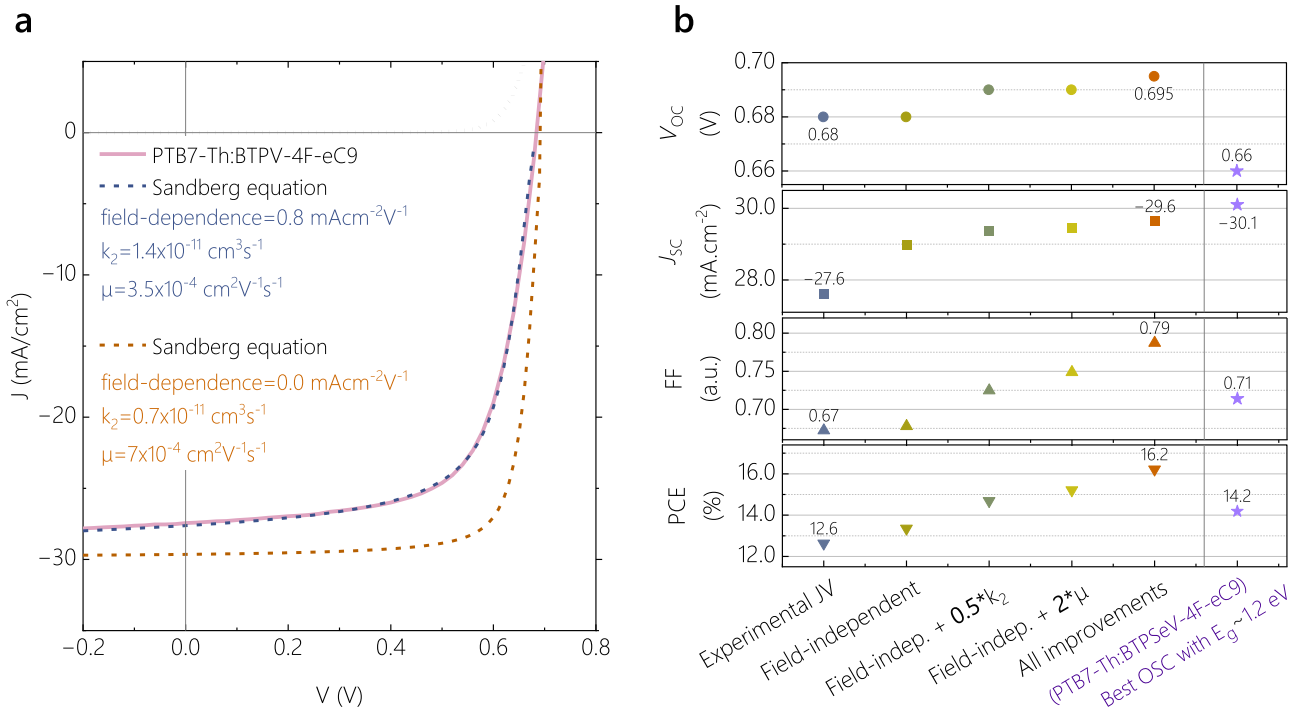

Figure 6. Validating the proposed bottlenecks to photocurrent and FF through *JV* simulations. a) Experimental *JV* curve of PTB7-Th:BTPV-4F-eC9, described perfectly by the diode equation from Sandberg et al. extended with a field bias-dependent free charge generation term (blue dotted line).[103] The input parameters to the diode equation are the experimentally determined bias-dependence of photocurrent, BMR coefficient k_2 and charge mobility μ, also shown in the legend. Predicted *JV*-characteristics are shown with the black dotted line, simulated without bias-dependence of photocurrent and a two-fold improvement to k_2 and μ. b) The photovoltaic metrics of PTB7-Th:BTPV-4F-eC9, for different *JV* cases reproduced with different input parameters, indicated in the *x*-axis. The values corresponding to the experimental case and the case for all improvements are obtained from the dotted *JV* simulations in the left-side figure. Also shown are the reported *JV* metrics for the highest-efficiency system around the 1.2 eV bandgap range (PTB7-Th:BTPSeV-4F-eC9).

losses.[28] Instead, the very good anticorrelation between EGE and PLQY suggested bias-dependent inefficient LE dissociation as its main cause for the poorer performance of this blend. Therefore, we conclude that photocurrent loss due to inefficient CT separation reported herein is not a general property of (low-offset) NFA blends, but instead that it is due to the unique properties of these low-bandgap NFAs and their aggregational tendencies owing to the presence of multiple stable molecular conformers.

To understand hypothetical performance limits, we used our experimental data to reproduce the *JV* curve of PTB7-Th:BTPV-4F-eC9 using the modified diode equation as recently reported by Sandberg et al.,[103] extended with a bias-dependent free charge generation term (see Figure S30, Supporting Information). Then, we propose incremental improvements to predict hypothetical PCEs that inch closer to the db-limit for this system. As seen in **Figure 6**a, the experimental *JV* curve of PTB7-TH:BTPV-4F-eC9 is perfectly reproduced by the extended Sandberg diode equation (blue dotted line). The input parameters, taken from our measurements of bias-dependence of free charge generation, recombination and mobility, are provided in the legend of Figure 6a. We now predict PCE enhancements by removing the bias-dependence term and proposing a two-fold improvement to either the mobility and recombination terms. The *JV* metrics associated therein are shown in Figure 6b, and the incremental *JV* curves in Figure S30 (Supporting Information). In the case that all three parameters are improved, the PCE for $E_g \approx 1.21$ eV can reach over 16% in theory. Indeed, Figure 6b shows that mitigating the bias-dependence of photocurrent unlocks the most potential increase in J_{SC} for this system. The *FF* is limited primarily by mobility, which ties to the disordered morphology of

Table 3. Summary of voltage loss analysis for the two low-bandgap OSCs.

System	$E_{gap,A}/q$ [V]	ΔV_{OC}^{rad} [V]	V_{OC}^{SQ} [V]	$\Delta V_{OC}^{rad,bg}$ [V]	V_{OC}^{rad} [V]	$\Delta V_{OC}^{non\text{-}rad}$ [V]	V_{OC} [V]	ΔV_{OC}^{total} [V]
PTB7-Th: BTPV-4Cl-eC9	1.22	0.25	0.97	0.03	0.94	0.29	0.65	0.57
PTB7-Th: BTPV-4F-eC9	1.24	0.25	0.99	0.04	0.95	0.27	0.68	0.56
PM6:Y6	1.39	0.27	1.12	0.05	1.07	0.26	0.84	0.55

the blend using this unique acceptor. This supports a recent report suggesting that realizing EQE>90% requires mobilities approaching 10^{-3} $cm^2V^{-1}s^{-1}$.[104] The predicted PCE lies within a realistic limit, considering the highest reported PCE of 14.2% for PTB7-Th:BTPSeV-4F-eC9.[9] Notably, this flagship system exhibits a larger J_{SC} owing to the smaller E_g ≈1.17. This system was also shown to have lower recombination than the non-selenated PTB7-Th:BTPV-4F-eC9, while its reported mobility of 4×10^{-4} $cm^{-2}V^{-1}s^{-1}$ and albeit marginal bias-dependence might be limiting higher FF, as indicated by the *JV* reproduced with the Sandberg equation (see Figure S30d, Supporting Information). All in all, our work highlights the need to mitigate field-dependence effects in low-bandgap OSCs in order to reach their photocurrent limits, while charge transport adds FF limits owing to morphological challenges posed by these low-bandgap materials. These results serve as a guideline for curbing challenges in pushing the PCE limits in state-of-the-art low-bandgap OSCs over 15% in order to realize their potential for tandem applications and beyond.

Supporting Information

Supporting Information is available from the Wiley Online Library or from the author.

Acknowledgements

A.S. and M.P. contributed equally to this work. The authors acknowledge funding support from the Deutsche Forschungsgemeinschaft (DFG, German Research Foundation) through the projects Fabulous (Project Number 450968074), Extraordinaire (Project Number 460766640) and Popular (Project Number 461909888). D.A. acknowledges funding by the Deutsche Forschungsgemeinschaft (DFG, German Research Foundation) for financial support through collaborative research centers (Grant Nos. TRR 146, SPP 2196, and 460766640). J.T.B and D.A. acknowledge support from the KAUST Office of Sponsored Research (OSR) under Award Nos. OSR-2018-CARF/CCF-3079 and OSR-CRG2018-3746. J.A.S. acknowledges financial support from the Australian Research Council (DE230100173). GIWAXS experiments were performed at NCD-SWEET beamline at ALBA synchrotron with the collaboration of ALBA staff. F.L. thanks the Volkswagen Foundation for funding through the Freigeist Program. D.B.R and A.A. acknowledge the financial support through the Welsh Government's Sêr Cymru II Program "Sustainable Advanced Materials" (Welsh European Funding Office – European Regional Development Fund) and by UKRI through the EPSRC Program Grant EP/T028513/1 Application Targeted and Integrated Photovoltaics and the UKRI Research England RPIF Programme (Centre for Integrative Semiconductor Materials).

Open access funding enabled and organized by Projekt DEAL.

Conflict of Interest

The authors declare no conflict of interest.

Data Availability Statement

The data that support the findings of this study are available in the supplementary material of this article.

Keywords

detailed balance, DFT calculations, geminate recombination, low bandgap, organic solar cells, photocurrent losses

Received: April 30, 2025
Revised: May 20, 2025
Published online:

[1] J. Fu, P. W. K. Fong, H. Liu, C. S. Huang, X. Lu, S. Lu, M. Abdelsamie, T. Kodalle, C. M. Sutter-Fella, Y. Yang, G. Li, *Nat. Commun.* **2023**, *14*, 19.
[2] J. Wang, Y. Wang, P. Bi, Z. Chen, J. Qiao, J. Li, W. Wang, Z. Zheng, S. Zhang, X. Hao, J. Hou, *Adv. Mater.* **2023**, *35*, 2301583.
[3] H. Lu, W. Liu, G. Ran, Z. Liang, H. Li, N. Wei, H. Wu, Z. Ma, Y. Liu, W. Zhang, X. Xu, Z. Bo, *Angew. Chem., Int. Ed.* **2023**, *62*, 202314420.
[4] Y. Jiang, S. Sun, R. Xu, F. Liu, X. Miao, G. Ran, K. Liu, Y. Yi, W. Zhang, X. Zhu, *Nat. Energy* **2024**, *9*, 975.
[5] C. Chen, L. Wang, W. Xia, K. Qiu, C. Guo, Z. Gan, J. Zhou, Y. Sun, D. Liu, W. Li, T. Wang, *Nat. Commun.* **2024**, *15*, 6865.
[6] D. Neher, *Nat. Res.* **2025**, *24*, 338.
[7] N. Schopp, H. M. Luong, B. R. Luginbuhl, P. Panoy, D. Choi, V. Promarak, V. V. Brus, T. Q. Nguyen, *ACS Energy Lett.* **2022**, *7*, 1626.
[8] N. Schopp, G. Akhtanova, P. Panoy, A. Arbuz, S. Chae, A. Yi, H. J. Kim, V. Promarak, T. Q. Nguyen, V. V. Brus, *Adv. Mater.* **2022**, 34, 2270226.
[9] Z. Jia, Q. Ma, Z. Chen, L. Meng, N. Jain, I. Angunawela, S. Qin, X. Kong, X. Li, Y. Yang, H. (Michael) Zhu, H. Ade, F. Gao, Y. Li, *Nat. Commun.* **2023**, *14*, 1236.
[10] Z. Jia, S. Qin, L. Meng, Q. Ma, I. Angunawela, J. Zhang, X. Li, Y. He, W. Lai, N. Li, H. Ade, C. J. Brabec, Y. Li, *Nat. Commun.* **2021**, *12*, 178.
[11] G. He, B. Mayberry, M. Pranav, M. S. Shadabroo, B. Sun, Y. Cao, S. Shoaee, M. Stolterfoht, D. Neher, F. Lang, *ACS Energy Lett.* **2023**, *8*, 3980.
[12] K. O. Brinkmann, T. Becker, F. Zimmermann, C. Kreusel, T. Gahlmann, M. Theisen, T. Haeger, S. Olthof, C. Tückmantel, M. Günster, T. Maschwitz, F. Göbelsmann, C. Koch, D. Hertel, P. Caprioglio, F. Peña-Camargo, L. Perdigón-Toro, A. Al-Ashouri, L. Merten, A. Hinderhofer, L. Gomell, S. Zhang, F. Schreiber, S. Albrecht, K. Meerholz, D. Neher, M. Stolterfoht, T. Riedl, *Nature* **2022**, *604*, 280.
[13] S. Zhang, F. Ye, X. Wang, R. Chen, H. Zhang, L. Zhan, X. Jiang, Y. Li, X. Ji, S. Liu, M. Yu, F. Yu, Y. Zhang, R. Wu, Z. Liu, Z. Ning, D. Neher, L. Han, Y. Lin, H. Tian, W. Chen, M. Stolterfoht, L. Zhang, W. H. Zhu, Y. Wu, *Science*, *380*, 404.
[14] S. S. Mali, J. V. Patil, J. A. Steele, M. K. Nazeeruddin, J. H. Kim, C. K. Hong, *Energy Environ. Sci.* **2023**, *17*, 1046.
[15] S. Wu, Y. Yan, J. Yin, K. Jiang, F. Li, Z. Zeng, S. W. Tsang, A. K. Y. Jen, *Nat. Energy* **2024**, *9*, 411.
[16] K. O. Brinkmann, P. Wang, F. Lang, W. Li, X. Guo, F. Zimmermann, S. Olthof, D. Neher, Y. Hou, M. Stolterfoht, T. Wang, A. B. Djurišić, T. Riedl, *Nat. Rev. Mater.* **2024**, *9*, 202.
[17] J. Lee, S. J. Ko, M. Seifrid, H. Lee, B. R. Luginbuhl, A. Karki, M. Ford, K. Rosenthal, K. Cho, T. Q. Nguyen, G. C. Bazan, *Adv. Energy Mater.* **2018**, *8*, 1801212.
[18] D. Liu, T. Wang, X. Ke, N. Zheng, Z. Chang, Z. Xie, Y. Liu, *Mater. Chem. Front.* **2019**, *3*, 2157.
[19] J. Hai, S. Luo, H. Yu, H. Chen, Z. Lu, L. Li, Y. Zou, H. Yan, *Mater. Adv.* **2021**, *2*, 2132.
[20] S. Qin, C. Lu, Z. Jia, Y. Wang, S. Li, W. Lai, P. Shi, R. Wang, C. Zhu, J. Du, J. Zhang, L. Meng, Y. Li, *Adv. Mater.* **2022**, *34*, 2108829.
[21] W. Liu, S. Sun, S. Xu, H. Zhang, Y. Zheng, Z. Wei, X. Zhu, *Adv. Mater.* **2022**,*34*, 2200337.
[22] O. Almora, G. C. Bazan, C. I. Cabrera, L. A. Castriotta, S. Erten-Ela, K. Forberich, K. Fukuda, F. Guo, J. Hauch, A. W. Y. Ho-Baillie, T. J. Jacobsson, R. A. J. Janssen, T. Kirchartz, R. R. Lunt, X. Mathew, D. B. Mitzi, M. K. Nazeeruddin, J. Nelson, A. F. Nogueira, U. W. Paetzold,

B. P. Rand, U. Rau, T. Someya, C. Sprau, L. Vaillant-Roca, C. J. Brabec, *Adv. Energy Mater.* **2024**, *14*, 2303173.
[23] R. Kerremans, C. Kaiser, W. Li, N. Zarrabi, P. Meredith, A. Armin, *Adv. Opt. Mater.* **2020**, *8*, 2000319.
[24] W. Li, S. Zeiske, O. J. Sandberg, D. B. Riley, P. Meredith, A. Armin, *Energy Environ. Sci.* **2021**, *14*, 6484.
[25] N. Liang, R. Tian, Y. Xu, H. Yao, H. Yang, Y. Wei, X. Xin, R. Chen, T. Zhai, Z. Wang, J. Hou, *Adv. Mater.* **2023**, *35*, 2300360.
[26] C. Yang, C. Zhao, Y. Sun, Q. Li, M. R. Islam, K. Liu, Z. Wang, S. Qu, Z. Wang, *Carbon Energy* **2021**, *3*, 4.
[27] L. Zhu, M. Zhang, G. Zhou, Z. Wang, W. Zhong, J. Zhuang, Z. Zhou, X. Gao, L. Kan, B. Hao, F. Han, R. Zeng, X. Xue, S. Xu, H. Jing, B. Xiao, H. Zhu, Y. Zhang, F. Liu, *Joule* **2024**, *8*, 3153.
[28] M. Pranav, A. Shukla, D. Moser, J. Rumeney, W. Liu, R. Wang, B. Sun, S. Smeets, N. Tokmoldin, Y. Cao, G. He, T. Beitz, F. Jaiser, T. Hultzsch, S. Shoaee, W. Maes, L. Luer, C. Brabec, K. Vandewal, D. Andrienko, S. Ludwigs, D. Neher, *Energy Environ. Sci.* **2024**, *17*, 6676.
[29] B. Sun, N. Tokmoldin, O. Alqahtani, A. Patterson, C. S. P. De Castro, D. B. Riley, M. Pranav, A. Armin, F. Laquai, B. A. Collins, D. Neher, S. Shoaee, *Adv. Energy Mater.* **2023**, *13*, 2300980.
[30] S. Karuthedath, J. Gorenflot, Y. Firdaus, N. Chaturvedi, C. S. P. De Castro, G. T. Harrison, J. I. Khan, A. Markina, A. H. Balawi, T. A. D. Peña, W. Liu, R. Z. Liang, A. Sharma, S. H. K. Paleti, W. Zhang, Y. Lin, E. Alarousu, D. H. Anjum, P. M. Beaujuge, S. De Wolf, I. McCulloch, T. D. Anthopoulos, D. Baran, D. Andrienko, F. Laquai, *Nat. Mater.* **2021**, *20*, 378.
[31] N. Tokmoldin, B. Sun, F. Moruzzi, A. Patterson, O. Alqahtani, R. Wang, B. A. Collins, I. McCulloch, L. Lüer, C. J. Brabec, D. Neher, S. Shoaee, *ACS Energy Lett.* **2023**, *8*, 2552.
[32] K. Nakano, Y. Chen, B. Xiao, W. Han, J. Huang, H. Yoshida, E. Zhou, K. Tajima, *Nat. Commun.* **2019**, *10*, 2520.
[33] D. Qian, S. M. Pratik, Q. Liu, Y. Dong, R. Zhang, J. Yu, N. Gasparini, J. Wu, T. Zhang, V. Coropceanu, X. Guo, M. Zhang, J. L. Bredas, F. Gao, J. R. Durrant, *Adv. Energy Mater.* **2023**, *13*, 2301026.
[34] A. Classen, C. L. Chochos, L. Lüer, V. G. Gregoriou, J. Wortmann, A. Osvet, K. Forberich, I. McCulloch, T. Heumüller, C. J. Brabec, *Nat. Energy* **2020**, *5*, 711.
[35] G. Zhou, M. Zhang, Z. Chen, J. Zhang, L. Zhan, S. Li, L. Zhu, Z. Wang, X. Zhu, H. Chen, L. Wang, F. Liu, H. Zhu, *ACS Energy Lett.* **2021**, *6*, 2971.
[36] H. Wu, H. Lu, Y. Li, X. Zhou, G. Zhou, H. Pan, H. Wu, X. Feng, F. Liu, K. Vandewal, W. Tress, Z. Ma, Z. Bo, Z. Tang, *Nat. Commun.* **2024**, *15*, 2693.
[37] M. Pranav, T. Hultzsch, A. Musiienko, B. Sun, A. Shukla, F. Jaiser, S. Shoaee, D. Neher, *APL Mater.* **2023**, *11*, 061111.
[38] J. S. Müller, M. Comí, F. Eisner, M. Azzouzi, D. Herrera Ruiz, J. Yan, S. S. Attar, M. Al-Hashimi, J. Nelson, *ACS Energy Lett.* **2023**, *8*, 3387.
[39] Y. Tamai, R. Shirouchi, T. Saito, K. Kohzuki, S. I. Natsuda, *J. Mater. Chem. A* **2023**, *11*, 17581.
[40] M. Saladina, P. Simón Marqués, A. Markina, S. Karuthedath, C. Wöpke, C. Göhler, Y. Chen, M. Allain, P. Blanchard, C. Cabanetos, D. Andrienko, F. Laquai, J. Gorenflot, C. Deibel, *Adv. Funct. Mater.* **2021**, *31*, 2007479.
[41] A. Y. Sosorev, D. Y. Godovsky, D. Y. Paraschuk, *Phys. Chem. Chem. Phys.* **2018**, *20*, 3658.
[42] H. Tamura, I. Burghardt, *J. Am. Chem. Soc.* **2013**, *135*, 16364.
[43] D. Di Nuzzo, L. J. A. Koster, V. S. Gevaerts, S. C. J. Meskers, R. A. J. Janssen, *Adv. Energy Mater.* **2014**, *4*, 1400416.
[44] K. Vandewal, S. Albrecht, E. T. Hoke, K. R. Graham, J. Widmer, J. D. Douglas, M. Schubert, W. R. Mateker, J. T. Bloking, G. F. Burkhard, A. Sellinger, J. M. J. Fréchet, A. Amassian, M. K. Riede, M. D. McGehee, D. Neher, A. Salleo, *Nat. Mater.* **2014**, *13*, 63.
[45] L. Perdigón-Toro, H. Zhang, A. Markina, J. Yuan, S. M. Hosseini, C. M. Wolff, G. Zuo, M. Stolterfoht, Y. Zou, F. Gao, D. Andrienko, S. Shoaee, D. Neher, *Adv. Mater.* **2020**, *32*, 1906763.
[46] J. Kurpiers, T. Ferron, S. Roland, M. Jakoby, T. Thiede, F. Jaiser, S. Albrecht, S. Janietz, B. A. Collins, I. A. Howard, D. Neher, *Nat. Commun.* **2018**, *9*, 2038.
[47] Y. Wu, Y. Li, B. van der Zee, W. Liu, A. Markina, H. Fan, H. Yang, C. Cui, Y. Li, P. W. M. Blom, D. Andrienko, G. J. A. H. Wetzelaer, *Sci. Rep.* **2023**, *13*, 4717.
[48] T. Fritsch, J. Kurpiers, S. Roland, N. Tokmoldin, S. Shoaee, T. Ferron, B. A. Collins, S. Janietz, K. Vandewal, D. Neher, *Adv. Energy Mater.* **2022**, *12*, 2200641.
[49] S. Yoon, N. Schopp, D. G. Choi, H. Wakidi, K. Ding, H. Ade, H. Vezin, G. N. M. Reddy, T.-Q. Nguyen, *Adv. Funct. Mater.* **2023**, *34*, 2308618.
[50] S. Ryu, N. Y. Ha, Y. H. Ahn, J. Y. Park, S. Lee, *Sci. Rep.* **2021**, *11*, 16781.
[51] S. Qin, Z. Jia, L. Meng, C. Zhu, W. Lai, J. Zhang, W. Huang, C. Sun, B. Qiu, Y. Li, *Adv. Funct. Mater.* **2021**, *31*, 2102361.
[52] J. Vollbrecht, J. Lee, S. J. Ko, V. V. Brus, A. Karki, W. Le, M. Seifrid, M. J. Ford, K. Cho, G. C. Bazan, T. Q. Nguyen, *J. Mater. Chem. C* **2020**, *8*, 15175.
[53] Y. Zhang, K. Liu, J. Huang, X. Xia, J. Cao, G. Zhao, P. W. K. Fong, Y. Zhu, F. Yan, Y. Yang, X. Lu, G. Li, *Nat. Commun.* **2021**, *12*, 4815.
[54] J. Yao, B. Qiu, Z. G. Zhang, L. Xue, R. Wang, C. Zhang, S. Chen, Q. Zhou, C. Sun, C. Yang, M. Xiao, L. Meng, Y. Li, *Nat. Commun.* **2020**, *11*, 2726.
[55] S. Shoaee, H. M. Luong, J. Song, Y. Zou, T. Q. Nguyen, D. Neher, *Adv. Mater.* **2023**, *36*, 2302005.
[56] T. Yanai, D. P. Tew, N. C. Handy, *Chem. Phys. Lett.* **2004**, *393*, 51.
[57] A. D. Becke, E. R. Johnson, *J. Chem. Phys.* **2005**, *123*, 154101.
[58] A. D. Becke, *J. Chem. Phys.* **1993**, *98*, 5648.
[59] E. R. Johnson, A. D. Becke, *J. Chem. Phys.* **2006**, *124*, 174104.
[60] F. Weigend, R. Ahlrichs, *Phys. Chem. Chem. Phys.* **2005**, *7*, 3297.
[61] E. R. Johnson, A. D. Becke, *J. Chem. Phys.* **2005**, *123*, 024101.
[62] S. Grimme, S. Ehrlich, L. Goerigk, *J. Comput. Chem.* **2011**, *32*, 1456.
[63] A. Markina, K. H. Lin, W. Liu, C. Poelking, Y. Firdaus, D. R. Villalva, J. I. Khan, S. H. K. Paleti, G. T. Harrison, J. Gorenflot, W. Zhang, S. De Wolf, I. McCulloch, T. D. Anthopoulos, D. Baran, F. Laquai, D. Andrienko, *Adv. Energy Mater.* **2021**, *11*, 2102363.
[64] Y. Fu, T. H. Lee, Y. C. Chin, R. A. Pacalaj, C. Labanti, S. Y. Park, Y. Dong, H. W. Cho, J. Y. Kim, D. Minami, J. R. Durrant, J. S. Kim, *Nat. Commun.* **2023**, *14*, 1870.
[65] D. Kroh, F. Eller, K. Schötz, S. Wedler, L. Perdigón-Toro, G. Freychet, Q. Wei, M. Dörr, D. Jones, Y. Zou, E. M. Herzig, D. Neher, A. Köhler, *Adv. Funct. Mater.* **2022**, *32*, 2205711.
[66] Y. Xiao, X. Lu, *Mater Today Nano* **2019**, *5*, 100030.
[67] R. Giridharagopal, P. A. Cox, D. S. Ginger, *Acc. Chem. Res.* **2016**, *49*, 1769.
[68] K. Jiang, Q. Wei, J. Y. L. Lai, Z. Peng, H. K. Kim, J. Yuan, L. Ye, H. Ade, Y. Zou, H. Yan, *Joule* **2019**, *3*, 3020.
[69] S. Tu, X. Lin, L. Xiao, H. Zhen, W. Wang, Q. Ling, *Mater. Chem. Front.* **2022**, *6*, 1150.
[70] A. Karki, J. Vollbrecht, A. J. Gillett, S. S. Xiao, Y. Yang, Z. Peng, N. Schopp, A. L. Dixon, S. Yoon, M. Schrock, H. Ade, G. N. M. Reddy, R. H. Friend, T. Q. Nguyen, *Energy Environ. Sci.* **2020**, *13*, 3679.
[71] T. A. D. Peña, R. Ma, Z. Xing, Q. Wei, J. I. Khan, R. M. Young, Y. Hai, S. A. Garcia, X. Zou, Z. Jin, F. L. Ng, K. L. Yeung, D. F. Swearer, M. R. Wasielewski, J. Wang, H. Cha, H. Yan, K. S. Wong, G. Li, M. Li, J. Wu, *Energy Environ. Sci.* **2023**, *16*, 3416.
[72] L. Perdigón-Toro, L. Q. Phuong, F. Eller, G. Freychet, E. Saglamkaya, J. I. Khan, Q. Wei, S. Zeiske, D. Kroh, S. Wedler, A. Köhler, A. Armin, F. Laquai, E. M. Herzig, Y. Zou, S. Shoaee, D. Neher, *Adv. Energy Mater.* **2022**, *12*, 2103422.
[73] T. Ferron, M. Waldrip, M. Pope, B. A. Collins, *J. Mater. Chem. A* **2019**, *7*, 4536.

[74] C. Wang, R. C. I. MacKenzie, U. Würfel, D. Neher, T. Kirchartz, C. Deibel, M. Saladina, *Adv. Energy Mater.* **2025**, 2405889.
[75] J. Kniepert, M. Schubert, J. C. Blakesley, D. Neher, *J. Phys. Chem. Lett.* **2011**, *2*, 700.
[76] B. Gerber, N. Tokmoldin, O. J. Sandberg, E. Sağlamkaya, B. Sun, S. Shoaee, D. Neher, *Sol. RRL* **2024**, *8*, 2400083.
[77] Y. Gao, J. Liao, H. Chen, H. Ning, Q. Wu, Z. Li, Z. Wang, X. Zhang, M. Shao, Y. Yu, *Adv. Sci.* **2023**, *10*, 2204727.
[78] C. Zhang, Y. Zhang, Z. Wang, Y. Su, Z. Wei, J. Hou, S. He, K. Wu, C. He, J. Zhang, C. Wang, *Sci. China Chem.* **2021**, *64*, 1569.
[79] A. Armin, M. Velusamy, P. Wolfer, Y. Zhang, P. L. Burn, P. Meredith, A. Pivrikas, *ACS Photonics* **2014**, *1*, 173.
[80] P. Dhakal, T. Ferron, A. Alotaibi, V. Murcia, O. Alqahtani, B. A. Collins, *J. Phys. Chem. Lett.* **2021**, *12*, 1847.
[81] R. Jasiūnas, H. Zhang, A. Devižis, M. Franckevičius, F. Gao, V. Gulbinas, *Sol. RRL* **2022**, *6*, 2100963.
[82] R. Wang, C. Zhang, Q. Li, Z. Zhang, X. Wang, M. Xiao, *J. Am. Chem. Soc.* **2020**, *142*, 12751.
[83] S. Giannini, D. J. C. Sowood, J. Cerda, S. Frederix, J. Grune, G. Londi, T. Marsh, P. Ghosh, I. Duchemin, N. C. Greenham, K. Vandewal, G. D'Avino, A. J. Gillett, D. Beljonne, *Mater. Today* **2023**, *80*, 308.
[84] D. B. Riley, O. J. Sandberg, W. Li, P. Meredith, A. Armin, *Phys. Rev. Appl.* **2022**, *17*, 024076.
[85] Z. Wang, Y. Guo, X. Liu, W. Shu, G. Han, K. Ding, S. Mukherjee, N. Zhang, H. L. Yip, Y. Yi, H. Ade, P. C. Y. Chow, *Nat. Commun.* **2024**, *15*, 1212.
[86] C. Sun, Z. Wu, Z. Hu, J. Xiao, W. Zhao, H. W. Li, Q. Y. Li, S. W. Tsang, Y. X. Xu, K. Zhang, H. L. Yip, J. Hou, F. Huang, Y. Cao, *Energy Environ. Sci.* **2017**, *10*, 1784.
[87] D. B. Riley, O. J. Sandberg, N. Zarrabi, Y. R. Kim, P. Meredith, A. Armin, *Adv. Mater.* **2023**, *35*, 2211174.
[88] S. I. Natsuda, T. Saito, R. Shirouchi, Y. Sakamoto, T. Takeyama, Y. Tamai, H. Ohkita, *Energy Environ. Sci.* **2022**, *15*, 1545.
[89] J. Kurpiers, D. Neher, *Sci. Rep.* **2016**, *6*, 26832.
[90] J. Kniepert, I. Lange, N. J. Van Der Kaap, L. J. A. Koster, D. Neher, *Adv. Energy Mater.* **2014**, *4*, 1301401.
[91] B. Sun, B. Gerber, S. Shoaee, D. Neher, *Sol. RRL* **2024**, *8*, 2400211.
[92] O. J. Sandberg, A. Sundqvist, M. Nyman, R. Österbacka, *Phys. Rev. Appl.* **2016**, *5*, 1301401.
[93] S. Wilken, D. Scheunemann, S. Dahlström, M. Nyman, J. Parisi, R. Österbacka, *Adv. Electron. Mater.* **2021**, *7*, 2001056.
[94] S. Shoaee, A. Armin, M. Stolterfoht, S. M. Hosseini, J. Kurpiers, D. Neher, *Sol. RRL* **2019**, *3*, 1900184.
[95] G. Zuo, S. Shoaee, M. Kemerink, D. Neher, *Phys. Rev. Appl.* **2021**, *16*, 034027.
[96] B. Philippa, M. Stolterfoht, P. L. Burn, G. Juška, P. Meredith, R. D. White, A. Pivrikas, *Sci. Rep.* **2014**, *4*, 5695.
[97] V. Coropceanu, J. L. Brédas, S. Mehraeen, *J. Phys. Chem. C* **2017**, *121*, 24954.
[98] D. Neher, J. Kniepert, A. Elimelech, L. J. A. Koster, *Sci. Rep.* **2016**, *6*, 24861.
[99] G. He, B. Mayberry, M. Pranav, M. S. Shadabroo, B. Sun, Y. Cao, S. Shoaee, M. Stolterfoht, D. Neher, F. Lang, *ACS Energy Lett.* **2023**, *8*, 3980.
[100] D. Qian, Z. Zheng, H. Yao, W. Tress, T. R. Hopper, S. Chen, S. Li, J. Liu, S. Chen, J. Zhang, X.-K. Liu, B. Gao, L. Ouyang, Y. Jin, G. Pozina, I. A. Buyanova, W. M. Chen, O. Inganäs, V. Coropceanu, J.-L. Bredas, H. Yan, J. Hou, F. Zhang, A. A. Bakulin, F. Gao, *Nat. Mater.* **2018**, *17*, 703.
[101] D. Baran, T. Kirchartz, S. Wheeler, S. Dimitrov, M. Abdelsamie, J. Gorman, R. S. Ashraf, S. Holliday, A. Wadsworth, N. Gasparini, P. Kaienburg, H. Yan, A. Amassian, C. J. Brabec, J. R. Durrant, I. McCulloch, *Energy Environ. Sci.* **2016**, *9*, 3783.
[102] S. M. Hosseini, S. Wilken, B. Sun, F. Huang, S. Y. Jeong, H. Y. Woo, V. Coropceanu, S. Shoaee, *Adv. Energy Mater.* **2023**, *13*, 2203576.
[103] O. J. Sandberg, A. Armin, *PRX Energy* **2024**, *3*, 023008.
[104] C. H. Tan, J. Zhang, T. Jia, W. Deng, Q. Wei, J. Zhang, H. Wu, Q. Xu, J. A. Röhr, F. Huang, Y. Ma, Y. Cao, *J. Phys. Chem. C* **2023**, *127*, 12135.